1 **High-precision atmospheric oxygen measurement comparisons between a newly built**

2 **CRDS analyzer and existing measurement techniques**

4 Tesfaye A. Berhanu[1,2], John Hoffnagle[2], Chris Rella[2], David Kimhak[2], Peter Nyfeler[1], Markus

5 Leuenberger[1]

6 [1]*Climate and Environmental Physics, Physics Institute and Oeschger Centre for Climate Change Research,*

7 *University of Bern, Bern, Switzerland*

8 [2]*Picarro Inc., 3105 Patrick Henry Drive, Santa Clara, CA, USA*

Abstract

11 Carbon dioxide and oxygen are tightly coupled in land-biospheres CO_2 - O_2 exchange

12 processes, while they are not coupled in oceanic exchange. For this reason, atmospheric

13 oxygen measurements can be used to constrain the global carbon cycle, especially oceanic

14 uptake. However, accurately quantifying the small (~1-100 ppm) variations in O_2 is

15 analytically challenging due to the very large atmospheric background which constitutes

16 about 20.9 % (~209500 ppm) of atmospheric air. Here we present a detailed description of the

17 analyzer and its operating principles as well as comprehensive laboratory and field studies for

18 a newly developed high-precision oxygen mixing ratio and isotopic composition analyzer

19 (Picarro G-2207) that is based on cavity ring-down spectroscopy (CRDS). From the

20 laboratory tests, we have calculated a short-term precision (standard error of one-minute O_2

21 mixing ratio measurements) of < 1 ppm for this analyzer based on measurements of eight

22 standard gases analyzed for two hours consecutively. In contrast to the currently existing

23 techniques, the instrument has an excellent long-term stability and therefore a calibration

24 every 12 hours is sufficient to get an overall uncertainty of < 5 ppm. Measurements of

25   ambient air were also conducted at the High-Altitude Research Station, Jungfraujoch and the

26   Beromünster tall tower in Switzerland. At both sites, we observed opposing and diurnally

27   varying CO_2 and O_2 profiles due to different processes such as combustion, photosynthesis

28   and respiration. Based on the combined measurements at Beromünster tower, we determined

29   height dependent O_2:CO_2 oxidation ratios varying between -0.98 to -1.60 , which increase

30   with the height of the tower inlet, possibly due to different source contribution such as natural

31   gas combustion with high oxidation ratio and biological processes which are at the lower end.

32   **1. Introduction**

33   Atmospheric oxygen comprises about 20.9 % of the global atmosphere and in the past decade

34   its concentration decreased at a rate of $\sim$ 20 per meg yr^{-1} (Keeling and Manning, 2014) mainly

35   associated with the increase in fossil fuel combustion. Measurements of atmospheric O_2 are

36   reported as the ratio to the N_2 concentration and expressed as $\delta(O_2/N_2)$ because the variations

37   in the concentrations of other atmospheric gases such as CO_2 can influence the O_2 partial

38   pressure while this ratio is insensitive to these changes in other gases. Atmospheric O_2 is

39   commonly expressed in units of per meg due to its small variability with respect to a large

40   background, where

$$\delta\left(\frac{O_2}{N_2}\right)(per\ meg) = \left(\frac{(\frac{O_2}{N_2})sample}{(\frac{O_2}{N_2})reference} - 1\right).10^6 \qquad (1)$$

42   Note that we convert per meg to parts per million equivalent by multiplying per meg by

43   0.209500 (the O_2 mole fraction of atmospheric air) (Machta and Hughes, 1970).

44   In contrast to O_2, the global average atmospheric CO_2 mixing ratio increased to 405.0 ppm

45   averaged over 2017 since its preindustrial value of 280 ppm (Le Quéré et al., 2017). As the

46   variability of atmospheric oxygen is directly linked to the carbon cycle, both its short and

47   long-term observations can be used to better constrain the carbon cycle. For example, since

48 first suggested by Keeling and Shertz (1992) the long-term trends derived from concurrent

49 measurements of atmospheric CO_2 and O_2 have been widely used to quantify the partitioning

50 of atmospheric CO_2 between the land-biosphere and oceanic sinks (Battle et al., 2000; Goto et

51 al., 2017; Manning and Keeling, 2006; Valentino et al., 2008). This method hinges on the

52 linear coupling between CO_2 and O_2 with an oxidation ratio (OR, defined as the

53 stoichiometric ratio of exchange during various process such as photosynthesis and respiration

54 expressed using α) of 1.1 for the terrestrial biosphere photosynthesis-respiration processes

55 (α_b) and 1.4 for fossil fuel combustion (α_f) while they are decoupled for oceanic processes (α_o

56 = 0). Meanwhile, the short-term variability in atmospheric oxygen can be used to estimate

57 marine biological productivity and air-sea gas exchange (Keeling et al., 1998; Nevison et al.,

58 2012). However, the accuracy of these estimates is primarily linked to the accuracy and

59 precision of atmospheric O_2 measurements and the assumed ORs for the different processes

60 which are highly variable in contrast to atmospheric CO_2 that can be well measured within the

61 precision guidelines set by the Global Atmospheric Watch (GAW) ($\pm$ 0.1 ppm for the

62 northern hemisphere).

63   Currently there are several, mostly custom built techniques that can measure

64 atmospheric O_2 variations as oxygen concentration based on interferometric, paramagnetic,

65 UV absorption and fuel cell technology (Keeling, 1988a; Manning et al., 1999; Stephens et

66 al., 2007) or as O_2/N_2 ratios to account for the large background effect using gas

67 chromatography with thermal conductivity detector (GC-TCD) or gas chromatography

68 coupled to mass spectrometry (GC-MS) (Bender et al., 1994; Tohjima, 2000). Despite the fact

69 that these techniques have been used for more than two decades, accurate quantification of

70 atmospheric oxygen variability remains challenging primarily because the small ppm-level

71 atmospheric oxygen signal rides on a ~ 210,000 ppm background, which places stringent

72 requirements on the precision and drift of the analysis methods especially for continuous

73 monitoring(note that the GAW recommendation for the measurement precision of O_2/N_2 is 2

74 per meg). The techniques listed above struggle to routinely achieve the necessary performance

75 for various reasons, including i) instability over time that requires frequent measurement

76 interruption for calibration, ii) measurement bias with ambient and sample temperature and/or

77 pressure, and/or iii) systematic errors in the measurement due to other atmospheric species.

78 Further, some techniques require the use of consumables and rely on high vacuum, which

79 complicates field deployment.

80   In this manuscript we describe a new high precision oxygen concentration and isotopic

81 composition analyzer by Picarro Inc., Santa Clara, USA (G-2207) based on CRDS

82 technology. Here, we will introduce the analyzer design principles in details, describe the

83 unique features of the analyzer and evaluate its performance based on various independent

84 laboratory and field tests by comparing it with currently existing techniques. Then, we will

85 present and interpret our observations based on field measurements. Finally, we will conclude

86 its overall performance and provide recommendations and possible improvements.

87 **2. Analyzer design principles**

88   The analyzer described here is derived from the Picarro G2000 series of CRDS

89 analyzers. The basic elements have been described elsewhere (Crosson, 2008; Martin et al.,

90 2016; Steig et al., 2014): briefly, the instrument is built around a high-finesse, traveling-wave

91 optical cavity, which is coupled to either of two single-frequency Distributed FeedBack-

92 stabilized semiconductor lasers. One cavity mirror is mounted on a piezoelectric translator

93 (PZT) to allow fine tuning of the cavity resonance frequencies. A semiconductor optical

94 amplifier between the laser sources and the cavity boosts the laser power and serves as a fast-

95 optical switch. The cavity body is constructed of invar and enclosed in a temperature

96   stabilized box (T = 45° C, stabilized to approximately 0.01 °C) for dimensional and

97   spectroscopic stability. A vacuum pump pulls the gas to be sampled through the cavity and a

98   proportional valve between the cavity and the pump maintains the sample pressure in the

99   cavity at a value of 340 hPa, with variations on the order of 1 Pa. The instrument has a

100   wavelength monitor, based upon measurements of interference fringes from a solid etalon,

101   which is used to control the laser wavelength by adjusting the laser temperature and current.

102   The wavelength monitor is a fiber-coupled device located between the laser and the cavity. A

103   fraction of the beam from the input fiber is collected using a beam splitter for the wavelength

104   measurement and the remaining power is collected in the output fiber. A high-speed

105   photodiode monitors the optical power emerging from the cavity. The instrument's data

106   acquisition system is used to sweep the laser frequency over the spectral feature to be

107   measured, modulates the laser output to initiate ring-downs, and fits the ring-down signal to

108   an exponential function to generate a spectrogram of optical loss versus laser frequency. For

109   this instrument the empty cavity ring-down time constant is about 39 μs. Subsequent program

110   modules compare the measured loss spectrum to a spectral model, using non-linear least-

111   squares fitting (Press et al., 1986) to find the best-fit model parameters and thereby obtain a

112   quantitative measure of the absorption due to the target molecule, and finally apply a

113   calibration factor to the optical absorption to deduce the molecular concentration. When

114   operating in its normal gas analysis mode, the instrument acquires about 200-300 ring-downs

115   per second and achieves a noise equivalent absorption of typically about 10^{-11} cm^{-1} Hz$^{-1/2}$,

116   with some variation between instruments.

117   The primary goal when designing this analyzer was to measure the molecular oxygen

118   concentration with few-per-meg level precision and stability. In this context operational

119   stability is as important as signal-to-noise. Our experience has been that the most stable

120 operation of the analyzer is achieved when the optical phase length of the cavity is held as

121 nearly constant as possible. In this case the free spectral range (FSR, 0.0206 cm^{-1}) of the

122 temperature stabilized, invar ring-down cavity provides a better optical frequency standard

123 than the etalon-based wavelength monitor, which in turn allows more consistent

124 measurements of absorption line width and integrated absorption line intensity (Steig et al.,

125 2014). For a small, field-deployable instrument, it is not practical to stabilize the absolute

126 frequencies of the cavity modes to an optical frequency standard (Hodges et al., 2004) but the

127 oxygen lines themselves, under conditions of constant temperature and pressure, provide an

128 adequate frequency reference. The oxygen spectrum was also used to calibrate the FSR, by

129 comparing a wide (approximately 10 cm^{-1}) FSR-spaced spectrum with the Hitran database

130 (Rothman et al., 2013).

131   To determine molecular oxygen concentration, the analyzer measures absorption of the

132 Q13Q13 component of the $a^1\Delta_g \leftarrow X^3\Sigma^-_g$ band, at 7878.805547 cm^{-1}, according to the latest

133 edition of Hitran (Gordon et al., 2017). This is one of the strongest near-infrared lines of

134 oxygen, well separated from other oxygen lines, and reasonably free of spectral interference

135 from water, carbon dioxide, methane, and other constituents of clean air. The spectral model

136 for this line was developed using reference spectra of clean, dry, synthetic air that were

137 acquired with the same hardware as in the field-deployable analyzer, but with special-purpose

138 software that allows it to operate as a more general spectrometer.

139   Recently, considerable work has been done to advance the understanding of spectral

140 line shapes and to define functional representations that better describe the processes that

141 determine spectral line shapes than does the Voigt model (Hartmann et al., 2008; Tennyson et

142 al., 2014, Tran et al., 2019). Line shape studies have been published for the 1.27 μm band of

143 O$_2$ (Fleisher et al., 2015; Lamouroux et al., 2014), though not to our knowledge for the Q

144 branch. The apparatus used here is not capable of spectroscopic studies of comparable

145 precision; the absolute temperature and pressure monitoring and especially the frequency

146 metrology are far too crude for that purpose. Our goal is merely to define a simple model of

147 the Q13Q13 line that is adequate for least-squares retrievals of the O_2 absorption under the

148 limited range of conditions (stabilized temperature and pressure) that the operational analyzer

149 experiences in the field. The CRDS analyzers use the Galatry function (Varghese and Hanson,

150 1984), which is distinctly better than the Voigt and still easily and quickly evaluated for line

151 shape modeling. Ultimately, the usefulness of the spectral model is to be evaluated by the

152 precision and stability of the O_2 measurements when compared with established techniques.

153 For spectral model development, this spectrometer has the drawback that the cavity FSR, is

154 too large to reveal much detail of the absorption line shape, even with the simplifying

155 assumption of a Galatry line shape. We therefore acquired a set of four interleaved spectra,

156 with the PZT-actuated mirror moved to offset the cavity modes of the individual FSR-spaced

157 spectra by one-fourth of an FSR. The precise offsets were determined from fits to the strong

158 and well-isolated O_2 lines in the spectra. From the consistency of the fitted line centers, we

159 estimate that the positioning of the interleaved spectra was accurate to approximately 10

160 MHz. The spectrum of the Q13Q13 line acquired in this manner is shown in Figure 1,

161 together with the best-fit Galatry function. It stands out that the residuals are largely odd in

162 detuning from the line center: this shows the limitations of the Galatry model in this case,

163 since the Galatry function is purely even about the line center. The shape of the absorption

164 line in this model is specified by two dimensionless parameters: the collisional broadening

165 parameter

166 $y = \gamma / \sigma_D$ (2)

167 and the collisional narrowing parameter

168      $z = \beta / \sigma_D$ (3)

169   where γ is the frequency of broadening transitions, β is the velocity change collision rate, and

170   σ_D is the 1/e Doppler half-width of the transition, given by

171      $\sigma_D = \nu_0 (2k_B T / Mc^2)^{1/2}$ (4)

172   where ν_0 is the transition frequency, k_B is Boltzmann's constant (J. K^{-1}), T is the sample

173   temperature (K), M is the molecular mass (amu), and c is the speed of light (m/s). Figure 2

174   shows the values of y and z obtained from spectra acquired in the same way as Figure 1, as a

175   function of cavity pressure. The values depend linearly on pressure, as expected from the

176   Galatry model, but the unconstrained linear fits do not go precisely through the origin. It is

177   not clear whether this represents a breakdown of the Galatry model or simply reflects the

178   limited quality of the data set. The slope of y can be converted to an air-broadened collisional

179   width γ_{air} = 0.0442 cm^{-1}/atm, which agrees with the Hitran value of 0.0460 cm^{-1}/atm (Gordon

180   et al., 2016) to within the uncertainty estimate stated by Hitran (uncertainty code 4 for γ_{air}

181   corresponding to 10% --20% relative uncertainty). The slope of z can be interpreted in terms of

182   the optical diffusion coefficient (Fleisher et al., 2015), yielding D = 0.285 cm^2 s^{-1}, compared

183   to the literature value of 0.233 cm^2 s^{-1} for O_2 in air at 45 °C (Marrero and Mason, 1972).

184   Although the anticipated use of the analyzer is for ambient air samples having a very small

185   range of O_2 concentrations, we did investigate the variation of the line shape in binary

186   mixtures of O_2 and N_2 shown in Figure 3. The error bars are taken from the output of the

187   Levenberg-Marquardt fitting routine (Press et al., 1992). The dependence of the collisional

188   broadening parameter z on O_2 mole fraction was considered too small to be significant, but

189   the variation in y was used in the subsequent analysis of the air samples. Note that Wójtewicz

190   et al. (Wójtewicz et al., 2014) also found collisional broadening coefficients for nitrogen to be

191   slightly larger than for oxygen in measurements of one O_2 line in the B-band.

192   The primary goal in designing the analyzer was to achieve high enough precision to

193   make meaningful measurements of O_2 in clean atmospheric samples. Although the current

194   best practice for such high-precision measurements is to work with dried samples, we decided

195   to include high precision measurements of water vapor. There were two reasons for this

196   decision: one is to serve as a monitor for residual water vapor, which is difficult to remove

197   completely from the ring-down cavity and associated sample handling hardware, and the

198   second and more ambitious reason was to see how well the effect of water vapor could be

199   corrected for measurements of undried ambient air. While it was considered unlikely that

200   measurements of undried air could compete in accuracy with those of dried air, it might be

201   possible to correct for water vapor well enough to enable useful measurements in some

202   circumstances without the expense and inconvenience of drying the sample. For this purpose,

203   a second laser was added, which probes the $7_{1,6} \rightarrow 8_{4,5}$ component of the $2v_3$ band of water

204   vapor, at of 7816.75210 cm^{-1} (Gordon et al., 2017). The Galatry model was used to fit spectra

205   of synthetic air humidified to various levels of water vapor concentration. These fits also

206   included two other nearby, very weak water lines, with intensities less than 1% of the strong

207   transition, in order that their absorption should not perturb the line shape of the main

208   transition. Results for the shape of the 7816.75210 cm^{-1} line are shown in Figure 4. At the

209   level that we can measure, only the y-parameter has a meaningful variation with water

210   concentration. From the linear fit one obtains a pressure broadening coefficient for air, $\gamma_{air} =$

211   0.0752 cm^{-1}/atm, in reasonable agreement with the Hitran value $\gamma_{air} = 0.0787$ cm^{-1}/atm

212   (Gordon et al., 2017), and a self-broadening coefficient $\gamma_{self} = 0.413$ cm^{-1}/atm, to be compared

213   with the Hitran value $\gamma_{self} = 0.366$ cm^{-1}/atm. Since the uncertainty estimate for the Hitran

214   values is 10 % to 20 %, this level of agreement seems reasonable.

We also looked at absorption from water near the Q13Q13 absorption line of O_2.
These spectra were measured in a background of pure nitrogen to reveal the very weak lines
interfering with the O_2 measurement. Without the strong O_2 lines, it was impossible to
interleave FSR-spaced spectra, so in this case the frequency axis comes from the analyzer's
wavelength monitor. The upper panel of Figure 5 shows the spectrum of saturated water vapor
in nitrogen, together with a fit to a Voigt model of the molecular lines. The measurement was
made at a pressure of 340 hPa and temperature of 45° C. The main features are the Q13Q13 line
from trace contamination of oxygen in the sample and several lines that arise from normal water
($^1H_2^{16}O$) and deuterated water ($^1H^2H^{16}O$ also abbreviated HDO). The lower panel of Figure 5 shows
the lines tabulated in Hitran. Immediately after the data in Figure 5 were acquired,
measurements were also made at 7816.85210 cm^{-1}, to establish the relationship between the
absorption strengths in the two spectral regions. The relative intensities of the H_2O and HDO
lines change with variations in the isotopic composition of the water, but fortunately the direct
interference with the oxygen Q13Q13 lines comes entirely from the H_2O isotopologue, with
the strongest HDO line being separated by approximately 8 line widths (FWHM) from the
Q13Q13 line. Hitran simulations for molecules other than water that are expected to be
present in clean, ambient air indicate that direct interference with the Q13Q13 line should be
negligible at the level of precision considered here. In the case of CO_2, the dilution of oxygen
due to 400 ppm of CO_2 is significant, and larger than any direct spectral interference.

Finally, we investigated the influence of water vapor on the shape of the O_2 Q13Q13
line. Switching between the two lasers sources, we acquired FSR-spaced spectra of
humidified synthetic air, alternately covering the 7817 cm^{-1} and 7878 cm^{-1} regions. Individual
spectra were acquired in less than 2 s, so changes in water vapor concentration between
spectra were small. These spectra, with frequency resolution of 0.0206 cm^{-1}, were analyzed by

239   nonlinear least-squares fitting with the following spectral models: the 7817 cm^{-1} spectra were

240   modeled as the sum of an empty-cavity baseline having an adjustable offset level and slope

241   and the water spectrum is modeled with three peaks: one strong line and two weak perturbers.

242   The molecular absorption of the main peak was expressed as an adjustable amplitude, A_w,

243   multiplying a dimensionless, area-normalized Galatry function (Varghese and Hanson, 1984).

244   The weak perturbers were modeled by Voigt profiles with amplitudes and line widths that

245   were constrained to be in fixed proportions to the strong line, and therefore added no new

246   degrees of freedom to the fitting procedure. Since the amplitude A_w multiplies an area-

247   normalized shape function, it is essentially equivalent to the area of the absorption line, to the

248   extent that the Galatry model provides a valid description of the line shape. The Doppler

249   width of the Galatry function was fixed based on the measured cell temperature, the y-

250   parameter was allowed to vary, and the z-parameter was constrained to be proportional to y,

251   based on measurements summarized in Figure 2. In addition, the center frequency of the

252   Galatry function was adjusted to match the data set, giving a total of five free parameters for

253   this fit. The 7878 cm^{-1} spectra were modeled with an adjustable baseline offset and slope and

254   molecular absorption amplitude, A_{O2}, describing the Q13Q13 O_2 line. Here, too, the y-

255   parameter and line center position of the O_2 lines were allowed to adjust, and the z-parameter

256   was constrained to be proportional to y. The weak water lines interfering with oxygen

257   absorption were included in the model, but with no additional free parameters; rather the

258   amplitudes were preset based on the measured water absorption at 7817 cm^{-1} and the

259   previously determined amplitude relationships between the water lines. This procedure does

260   not account for variations in HDO abundance, which may introduce some systematic error

261   into the water vapor correction for samples of unusual isotopic composition, but it should

262   accurately model the most important lines that interfere with the oxygen measurement.

263 Collisional broadening of the Q13Q13 O_2 line by water vapor is shown in Figure 6. From the

264 linear fit one obtains a coefficient for collisional broadening of the Q13Q13 line by water

265 vapor of γ_{water} = 0.0442 cm^{-1}/atm at 45 °C. Recently, parameters describing broadening of

266 oxygen lines by water vapor, obtained by empirical modeling of selected experimental

267 data, were added to the Hitran data base (Tan et al., In review). The new Hitran entries predict

268 a value of 0.0486 cm-1/atm at 45 °C, which is in agreement with our measurement within the

269 5-10% uncertainty attributed by Hitran to the broadening parameter. The alternating

270 measurements at 7817 cm^{-1} and 7878 cm^{-1} also calibrated the relationship between water mole

271 fraction and the absorption at 7817 cm^{-1}, using a dilution analysis described by Filges et al.

272 (2018), who showed that the results obtained this way agree well with water vapor fractions

273 measured with a conventional hygrometer. Figure 7 shows the measured amplitudes of the

274 water and oxygen lines for samples of variable humidity. Since the air came from a tank of

275 constant composition, the oxygen concentration changes due to dilution of oxygen when

276 water is added. Assuming that this is the sole cause of the change in measured absorption,

277 since the line shapes were being constantly adjusted to account for changes in collisional

278 broadening, it is straightforward to deduce the relation between the water fraction and the

279 absorption amplitude. This calibration was used to generate the water fraction axes in Figures

280 4 and 6. We note that we did not take particular care to control or measure the quantity of

281 dissolved gases, especially oxygen and carbon dioxide, in the water used for this experiment.

282 While these gases would not significantly affect the water calibration, they may affect the

283 water vapor correction of the oxygen measurement at the ppm level. More work needs to be

284 done to investigate the water vapor correction of the oxygen measurement.

285 The observations described above were used to design a method to measure oxygen

286 concentration in ambient air. Gas from the inlet to the analyzer is drawn through the cavity at

287   a rate of about 100 sccm (standard cubic centimeter per minute) and the conditions in the

288   cavity are held stable at 340 hPa and 45°C. In its analysis mode the analyzer alternately

289   measures ring-downs in the 7817 cm^{-1} and 7878 cm^{-1} regions. At 7878 cm^{-1} measurements are

290   made at 11 different frequencies, spaced by one FSR of the cavity and centered at the peak of

291   the Q13Q13 line. Multiple ring-down measurements are made to improve the precision of the

292   loss determination, with a total of 305 ring-downs allocated to one spectrum. In the 7817 cm^{-1}

293   region measurements are also made at 11 distinct frequencies at FSR spacings. Only 35 ring-

294   downs are allocated to this spectral region, since the measurement of O_2 is much more

295   important than water vapor. The data sets are analysed using a Levenberg-Marquardt fitting

296   routine, which adjusts five free parameters in each region to find the best agreement to a

297   spectral model based on Galatry line shapes, as described above. One of the outputs of the

298   7878 cm^{-1} fit is the frequency offset of the FSR grid from the center of the Q13Q13 line. This

299   information is used to adjust the position of the PZT actuated mirror to keep the

300   measurements centered on the line, effectively stabilizing the optical path length of the cavity

301   to the frequency of the O_2 line. The reported water fraction is obtained by multiplying the

302   fitted amplitude of the water line by a calibration constant derived from the dilution

303   experiment as explained above. For the O_2 fraction a slightly more complicated procedure is

304   followed. It was observed that the least-squares fitting of the data gives highly correlated

305   results for the amplitude of the absorption line and the line width parameter y. The correlation

306   may be due in part to covariance of the fitted amplitude (proportional to line area) and line

307   width (Press et al., 1992) and it may also have a contribution from pressure variations that the

308   pressure sensor is unable to detect. The ratio A_{O2}/y can be determined from the fit much more

309   precisely than A_{O2} alone and so gives a more sensitive measurement of molecular absorption.

310   It also has the advantage of being independent of sample pressure, to the extent that the

Galatry model applies (Figure 2). However, using the ratio A_{O2}/y as a metric for absorption adds more complications if measurements are to be made over a range of O_2 and water concentrations, because the O_2/N_2 ratio and the water concentration affect the line width independently of pressure and O_2 concentration alone. To minimize systematic errors due to these broadening effects, we define a nominal y-parameter based on the measured amplitudes of the O_2 and water lines and the line broadening dependences shown in Figures 3 and 4. The measured ratio A_{O2}/y is normalized by the nominal y to obtain a quantity that is ideally independent of pressure and water concentration, and this is the quantity that is multiplied by a calibration constant to give the reported O_2 fraction. In addition, a dry mole fraction is reported for O_2, defined as the directly measured mole fraction corrected for water dilution.

The main goal in developing this instrument was to make high precision measurements of O_2 mole fraction, based on absorption by the dominant $^{16}O_2$ isotopologue. The absorption lines of the rarer isotopologues are also present nearby, so a mode of operation was included in which one laser is scanned over neighboring lines of $^{16}O_2$ and $^{16}O^{18}O$ and the ratio of amplitudes is used to derive an isotopic ratio, reported in the usual delta notation. In this case the operating pressure was reduced to 160 hPa to improve the resolution of the nearby lines. The lines measured were the Q3Q3 line of $^{16}O_2$, at 7882.18670 cm^{-1}, and the Q9Q9 line of $^{16}O^{18}O$, at 7882.050155 cm^{-1}. The measurement procedure is very much like that for the O_2 fraction measurement, so it will not be described in detail, only the main differences will be noted. One is that in determining an isotopic ratio, normalizing absorption amplitudes by line widths does not provide any advantage, instead we simply take the ratio of amplitudes to compute delta. Although the Q9Q9 line and its neighbor Q8Q8 are the strongest ones in this band, absorption by $^{16}O^{18}O$ is still very weak, only about 5×10^{-9} cm^{-1} at the line center under the conditions we used. The signal-to-noise that can be achieved with this

335 analyzer is not adequate to determine both the amplitude and the width of the $^{16}O^{18}O$ line with

336 useful precision, so in the fitting step the y-parameter of the $^{16}O^{18}O$ line is constrained to be a

337 constant factor times the fitted y-parameter for the $^{16}O_2$ line. Additionally, because of the

338 weakness of the rare isotopologue absorption, the majority of ring-downs in each spectrum is

339 devoted to measuring $^{16}O^{18}O$ i.e. 232 ring-downs in each spectrum versus only 40 for $^{16}O_2$.

340 This implies that the mole fraction measurement in the isotopic mode is much less precise

341 than when the analyzer measures the Q13Q13 line alone.

3. Results and Discussions

3.1. Laboratory tests at Picarro, Santa Clara

344 3.1.1. Temperature and pressure sensitivity

345   One set of tests was done to determine how well the goal was met of minimizing the

346 susceptibility of the concentration measurements to noise or drift of the sample temperature

347 and pressure. For these tests the analyzer sampled dry synthetic air from a tank and the

348 temperature and pressure setpoints of the cavity were adjusted upward and downward from

349 the nominal values, to obtain an estimate of the differential response. We express the

350 sensitivity to experimental conditions in relative form, that is the derivative with respect to

351 temperature or pressure divided by the signal under nominal conditions.

352   From these experiments, we determined a temperature sensitivity of -2.1×10^{-4} K^{-1} and

353 a pressure sensitivity of $+9.8 \times 10^{-6}$ hPa^{-1}. The temperature sensitivity is somewhat larger than

354 expected based on a calculation using Hitran data to estimate the temperature dependences of

355 all the quantities that go into the measured absorption of the Q13Q13 line. The pressure

356 sensitivity is strikingly small, indicating a good cancelation of the pressure dependence of

357 absorption amplitude and line width. Both temperature and pressure sensitivities are small

358 enough to have a negligible effect on short-term precision of measurements made with the

359   stabilized ring-down cavity, though long-term drifts in the sensors are always a matter of

360   concern.

361   3.1.2. Measurement precision and drift

362   Measurement precision was evaluated by analyzing synthetic air containing nominal

363   atmospheric concentrations of CO_2 and CH_4 from an aluminum Luxfer cylinder over a period

364   of several days. The tank, oriented horizontally and thermally insulated (though not

365   controlled), was connected directly to the instrument (S/N TADS2001) with a 2-stage

366   pressure regulator and stainless-steel tubing with an additional orifice to about 55 sccm. For

367   the isotopic mode of operation, the precision of the measurement was also tested by making

368   repeated measurements from a tank of clean, dry synthetic air.

369   Figure 8 shows the time series of the precision test data, displaying the reported

370   oxygen concentration, the height of the oxygen absorption peak, the width of the oxygen

371   absorption peak and the ambient temperature. The residual error of the analyzer, although

372   small, is nevertheless significant given the stringent targets set forth by the WMO-GAW

373   program. Possible sources of error include: temperature drifts due to sensor drift or gradients;

374   pressure errors due to sensor drift; optical artifacts such as parasitic reflections, higher order

375   cavity mode excitation, and/or loss nonlinearity that can distort the reported oxygen spectrum.

376   More work is required to identify and eliminate these small drifts.

377   The Allan standard deviation of the reported O_2 fraction is shown in the Allan-Werle

378   plot in Figure 9. The ordinate on this plot is the square root of the Allan variance of reported

379   mole fraction, so 1 ppm in these units corresponds to about 5 per meg in the ratio of O_2/N_2.

380   The precision of averaged measurements improves as $\tau^{-1/2}$ for approximately 5000 s and

381   reaches 1 ppm in less than 10 minutes and remains below 1 ppm for time scales on the order

382   of about 1 hour (τ is the averaging time which is the abscissa of the Allan-Werle plot).

383   Figure 10 shows the precision of $\delta(^{18}O)$ (uncalibrated) derived from the ratio of lines

384   measured at 7882 cm^{-1}. Because of the weak signal from the $^{16}O^{18}O$ line, it is necessary to

385   average for more than 20 seconds or more to achieve 1‰ precision on the isotopic ratio. As

386   for the concentration measurement, averaging improves the measurement precision for time

387   scales up to about 1 hour.

3.2. Laboratory measurements at the University of Bern

389   3.2.1. Measurements of standard gases

390   The performance of the instrument was tested by analyzing eight standard gases with

391   precisely known CO_2 and O_2 compositions (Table 1) using the CRDS analyzer and comparing

392   it to parallel measurements with a paramagnetic oxygen sensor (PM1155 oxygen transducer,

393   Servomex Ltd, UK) embedded to a commercially available fuel cell oxygen analyzer

394   (OXZILLA II, Sable Systems International, USA) (Sturm et al., 2006) as well as with an

395   isotope ratio mass spectrometer (IRMS, Finnigan Delta^{Plus}XP). The design of the

396   measurement set-up is shown in Figure 11. Standard gases were directly connected to the

397   pressure controlling unit, and a multi-port valve (V2) was used to select among the standard

398   gases. Flow from each cylinder was adjusted to about 120 sccm which was eventually

399   directed to a selection valve (V1), allowing switching between ambient air and standard gases.

400   Flow towards and out of the fuel cell analyzer was controlled by the pressure controlling unit.

401   The O_2 mixing ratio of this incoming gas was first measured on the Paramagnetic O_2 sensor

402   and then directed towards a non-dispersive infrared analyzer (NDIR) (Li-7000, LICOR, USA)

403   for measuring CO_2 and H_2O. The outflow from this analyzer (100 sccm) returns to the

404   pressure controlling unit and was eventually divided between the CRDS analyzer (which uses

405   about 75-80 sccm) and the IRMS (~ 20 sccm) via a Tee-junction. Each cylinder was measured

406   for two hours in each system controlled by a LabView program.

407   First, we investigated the influence of this Tee-junction, which splits the gas flow

408   between the CRDS and the IRMS, on the measured O_2 values. Manning (2001) showed that

409   the fractionation of O_2 in the presence of a Tee-Junction is strongly dependent on the splitting

410   ratios as well as temperature and pressure gradients. Hence, we measured and compared the

411   O_2 mixing ratios of two standard gases (CA07045 and CA060943) in two cases: i) in the

412   presence of a Tee-junction with different CRDS to IRMS splitting ratios and ii) without a

413   Tee-junction so that all gas flow is directed towards the CRDS analyzer. The splitting ratios in

414   these test experiments vary from 1:1 to 1:100, and reversed to change the major flow direction

415   either to the CRDS or the IRMS. Note that the experimental condition in this manuscript is

416   with a 4:1 splitting ratio (i.e. ~ 80 sccm towards the CRDS analyzer and ~ 20 sccm towards

417   the IRMS).

418   In the cases of the smaller splitting ratios (1:1, 1:4 and 4:1), which are relevant for the

419   results presented in this study, only minor differences in the measured O_2 mixing ratios were

420   observed when compared to case ii (i.e. without a Tee-junction). For these two cylinders

421   measured, the average differences in these cases were about 0.5 ppm, calculated as the mean

422   of the differences in the raw O_2 measurements of the last 60 seconds. The negligible

423   fractionation can indeed be the result of smaller splitting ratios while strong influence is

424   usually expected in case of larger splitting ratios (Stephens et al., 2007). For higher splitting

425   ratios, the result seems inconclusive without any dependence on the ratios due to the strong

426   decline in the cylinder temperature (specifically at the pressure gauge) caused by higher flow

427   to achieve the higher splitting ratios (as high as 1:100). Hence, these tests need to be

428   conducted in a temperature-controlled condition and the results could not be discussed in this

429   manuscript.

430   Figure 12 shows the standard gas measurements for the seven cylinders with known

431   CO_2 and O_2 mixing ratios (Table 1) using both the CRDS and the Paramagnetic analyzers.

432   Standard eight, which has too high O_2, is not shown in the figure as the figure is zoomed-in to

433   better illustrate the change in O_2 for the remaining cylinders. While the first five cylinders

434   contain O_2 and CO_2 mole fractions comparable to ambient air values, standards 6 & 8 had

435   either very low or very high O_2, respectively. In addition, standards 6 and 7 have very low and

436   very high CO_2 mixing ratios. Note that due to its very high CO_2 content (~ 2700 ppm),

437   standard 7 was not measured on the IRMS and hence the O_2 mixing ratio is unknown. The

438   measured mixing ratios for the six standard gases measured with the two systems are in very

439   good agreement while cylinder 7 showed an opposing signal for the two analyzers compared

440   to standard 6 (Figure 12). While the Paramagnetic analyzer showed a higher O_2 mixing ratio,

441   the values from the CRDS analyzer are lower in O_2. This can be associated with the very high

442   CO_2 mixing ratio in standard 7, which leads to a strong dilution effect in the CRDS analyzer

443   as it does not include any correction function for dilution effect from CO_2. However, such

444   high CO_2 mixing ratios may not be that important for most atmospheric research. Yet, it

445   should be considered to include a parallel CO_2 mixing ratios measurement to the instrument

446   as it will further improve the accuracy. This would be especially important for biological or

447   physiological studies where a wide range of CO_2 and O_2 concentrations must be expected.

448   The measurement precision of the CRDS analyzer was calculated as the standard error

449   of the mean i.e. the standard deviation ($1\text{-}\sigma$) of the last 1-minute raw measurements divided

450   by the square root of the number of measurements ($n = 60$), and for all these cylinders the

451   values are usually between 0.5 ppm to 0.7 ppm. For parallel measurements of these cylinders

452   using a Paramagnetic analyzer, we obtained a precision of about 1 ppm, calculated exactly the

453   same way.

454   We also made a correlation plot to see which of the two instruments are in better

455   agreement with the assigned values based on IRMS measurements for the individual

456   cylinders. While similar correlation coefficients were observed for both analyzers, different

457   slopes were calculated (Fig. A.1). This is due to the fact that the IRMS measures the O_2 to N_2

458   ratio ($\delta(O_2/N_2)$) in per meg, while the CRDS and the Paramagnetic analyzers provide non-

459   calibrated O_2 mixing ratios in units of ppm and per meg, respectively. If we exclude the two

460   standard gases with the highest and lowest O_2 mixing ratios (standards 7 and 8) that are

461   subjected to strong dilution effects, both the slope and the r^2 values decrease from those

462   shown in Figure A.1. But this decrease is larger in the case of the Paramagnetic

463   measurements, implying a slightly better linearity of the CRDS analyzer.

464   3.2.2. Measurements of ambient air

465   Ambient air measurements were conducted from the roof top of our laboratory at the

466   University of Bern to evaluate the analyzer's performance under atmospheric variability.

467   Ambient air was continuously aspirated from the inlet at the roof of the building at a flow rate

468   of ~ 250 sccm which is then dried using a cooling trap kept at -90 °C towards the switching

469   valve (V1) and measured in similar way to the standard gases as explained above. The

470   measurement values obtained here were compared with the parallel measurements by the

471   Paramagnetic sensor to test the instruments stability and accuracy.

472   Figures 13 panels a &b show the 1-minute average ambient air measurements from the

473   rooftop inlet by the Paramagnetic and the CRDS analyzers at the beginning of the testing

474   period including standard gases measured every 12-hour. While the Paramagnetic analyzer

475   seems to be stable, the CRDS analyzer showed a strong drift for an extended period. This can

476   be due to unstable conditions in the CRDS measurement system as it started operating right

477   after it was unpacked. Hence, we looked into temperature inside the instrument chassis and

478   pressure records, which were stable within the manufacturer's recommended range during this

479   period. As the CRDS analyzer incorporates a water correction function, interference from this

480   species should be well accounted. Even comparing the analyzer's parallel water

481   measurements to water measurements by the NDIR system such a drift was not observed. It

482   should be noted that the two internal standard gases which were less frequently measured

483   (every 12 hours) during this period were also drifting following similar pattern. This implies

484   that the drift is associated with the analyzer. Interestingly, this pattern can be modeled using a

485   polynomial function which can then be used to correct for the observed drift in the ambient air

486   measurements. After applying a polynomial drift correction, we were able to fully accounted

487   for the observed drift. However, the manufacturer decided to further investigate possible

488   causes of this drift. After further improvements, we obtained the first commercial analyzer in

489   September 2017 and repeated the above tests (Figure 13 c &d). No such drift was observed

490   any more in the standard gases or in ambient air measurements.

491   We believe that the optical amplifier has caused the drift in the first system and not anymore

492   included in the design of the product which produced a significant amount of broadband light

493   that could fill the cavity (albeit with a low coupling coefficient), and would ring down with a

494   different (and generally much faster) time constant that the baseline loss of the cavity.

495   However, the ringdown time on the peak of the oxygen line is just 10 microseconds, such that

496   the broadband light might have distorted the single exponential decay of the central laser

497   frequency, leading to the observed drift in the oxygen signal. However, we were not able to

498   confirm this hypothesis.

499   3.2.3. Water correction test

500   Measurements of oxygen are reported as both wet ($O_{2,\ raw}$) and dry ($O_{2,\ dry}$) mole

501   fractions by the CRDS analyzer as it also measures water vapor in parallel at its water

502   absorption line (7817 cm^{-1}), and corrects for the dilution effect based on an inbuilt numerical

503   function:

504   $$O_{2,dry} = \frac{O_{2,raw}}{1-f_{H_2O}} \qquad\qquad (5)$$

505   where f_{H2O} is the measured water mole fraction.

506   The efficiency of water correction by this function was assessed in two ways: i) by comparing

507   the water vapor content in standard air measured by this analyzer with similar measurements

508   by the NDIR analyzer and ii) by comparing the oxygen mixing ratios between non-dried

509   ambient air measured and corrected for water dilution by the CRDS analyzer with dried air

510   measured using a paramagnetic analyzer.

511   Figure 14 shows the water vapor content for standard gases measured continuously for

512   two days by the CRDS and the NDIR analyzers. Note that the two data sets are manually

513   fitted to each other as the measured water values by the NDIR analyzer are not calibrated.

514   Based on this plot, the two analyzers are in very good agreement although there are small

515   differences during very dry conditions (low water content).

516   Figure 15a shows the dried ambient air water measurements in both analyzers with

517   frequent spikes due to valve switching while measuring standard gases. In the second case,

518   where the water trap was by-passed and non-dried air was allowed to the CRDS analyzer

519   keeping the dried air flow to the NDIR (Figure 15b), a clear increase in the water

520   measurements in the CRDS analyzer can be observed. Here, it should be noted that there are

521   no spikes in the water measurements of the CRDS analyzers as there are no standard gas

522   measurements in between and the inlet is directly connected to the CRDS analyzer (Figure

523   11). Figures 15c & 15d show the difference in oxygen measurements of ambient air measured

524   in both analyzers in the two cases stated above (note that the CRDS uses its built-in water

correction function applying Eq. 5). The measurements of the Paramagnetic analyzer were scaled to ppm units by applying the correlation equation obtained from the six standard gas measurements of the two analyzers (Fig. A.1). Note that the CRDS measurements were corrected for the observed drift using the polynomial fit to the two standard gas measurements stated above.

In the first period of the measurement when both analyzers measured dried ambient air, the absolute differences between the 1-minute averages measured over two days by the two analyzers were mostly within 15 ppm (Figure 15c) and symmetrically distributed around zero (Figure 15e). However, when wet air was admitted to the CRDS analyzer and the in-built water correction was applied, a stronger variability was observed in the calculated differences (Figure 15d). This implies stronger short term variability in the CRDS analyzer measurement values (as nothing was changed for the Paramagnetic measurement system) when wet samples were analyzed. The more negative values in the differences (Figure 15f) can also be associated with overestimation of the O_2 mixing ratios by the CRDS originating from an overestimated water correction. However, detailed evaluation of the analyzer's water correction function is beyond the scope of this study.

3.3. Field Measurements

After a series of tests at University of Bern, we conducted multiple field measurements at the High Altitude Research Station Jungfraujoch and the Beromünster tall tower sites in Switzerland described below.

3.3.1. Tests at the High Altitude Research station Jungfraujoch

The High Alpine research station Jungfraujoch is located on the northern ridge of the Swiss Alps (46° 33′ N, 7° 59′ E) at an elevation of 3580 m a.s.l. It is one of the global atmospheric watch (GAW) stations well-equipped for measurements of numerous species and

549 aerosols. The site is above the planetary boundary layer most of the time due to its high

550 elevation (Henne et al., 2010; Zellweger et al., 2003). However, thermally uplifted air from

551 the surrounding valleys during hot summer days or polluted air from the heavily industrialized

552 northern Italy may reach at this site (Zellweger et al., 2003). The Division of Climate and

553 Environmental Physics at the University of Bern has been monitoring CO_2 and O_2 mixing

554 ratios at this site based on weekly flask sampling and continuous measurements since 2000

555 and 2004, respectively (Schibig et al., 2015). The CO_2 mixing ratio is measured using a

556 commercial NDIR analyzer (S710 UNOR, SICK MAIHAK) while O_2 is measured using the

557 Paramagnetic sensor (PM1155 oxygen transducer, Servomex Ltd, UK) and fuel cells (Max-

558 250, Maxtec, USA) installed inside a home-built controlling unit. Similar to the comparison

559 tests at the University of Bern, we have conducted parallel measurements between the CRDS

560 analyzer and the paramagnetic cell at this high altitude site during 03 – 14 February 2017. The

561 measurement of ambient air at the Jungfraujoch system is composed of sequential switching

562 between low span (LS) and high span (HS) calibration gases followed by a target gas (T)

563 measurement (once a day) to evaluate the overall system performance and finally a working

564 gas (WG) measurement before switching back to ambient air.

565 Figure 16 (top panel) shows the calibrated 1-minute averaged O_2 mixing ratios

566 measured at this high altitude site in comparison with the Paramagnetic oxygen analyzer

567 already available at the site. Despite the strong variability observed during the measurement

568 period of 10-days by both analyzers, a very good agreement was observed between them.

569 Figure 16 (bottom panel) shows the absolute difference of 1-minute averages in

570 atmospheric O_2 measured at Jungfraujoch between the two analyzers which are mostly within

571 ± 5 ppm range (but sometimes going as high as ± 10 ppm) without an offset. However, for

572   generally reported 10-minutes, half-hourly or hourly means these values correspond to < 1.5

573   ppm, < 1 ppm and < 0.65 ppm.

574   3.3.2. Tests at the Beromünster tall tower site

575   The Beromünster tower is located near the southern border of the Swiss Plateau, the

576   comparatively flat part of Switzerland between the Alps in the south and the Jura mountains

577   in the northwest (47° 11′ 23″ N, 8° 10' 32″ E, 797 m a.s.l.), which is characterized by intense

578   agriculture and rather high population density. A detailed description of the tower

579   measurement system as well as a characterization of the site with respect to local

580   meteorological conditions, seasonal and diurnal variations of greenhouse gases, and regional

581   representativeness can be obtained from previous publications (Berhanu et al., 2016; Berhanu

582   et al., 2017; Oney et al., 2015; Satar et al., 2016). The tower is 217.5 m tall with access to five

583   sampling heights (12.5 m, 44.6 m, 71.5 m, 131.6 m, 212.5 m) for measuring CO, CO_2, CH_4

584   and H_2O using Cavity Ring Down Spectroscopy (Picarro Inc., G-2401). By sequentially

585   switching from the highest to the lowest level, mixing ratios of these trace gases were

586   recorded continuously for three minutes per height, but only the last 60 seconds were retained

587   for data analysis. The calibration procedure for ambient air includes measurements of

588   reference gases with high and low mixing ratios traceable to international standards (WMO-

589   X2007 for CO_2 and WMO-X2004 for CO and CH_4), as well as target gas and more frequent

590   working gas determinations to ensure the quality of the measurement system. From two years

591   of data a long-term reproducibility of 2.79 ppb, 0.05 ppm, and 0.29 ppb for CO, CO_2 and

592   CH_4, respectively was determined for this system (Berhanu et al., 2016).

593   Between 15.02.2017 and 02.03.2017, we have connected the new CRDS oxygen

594   analyzer in series with the CO_2 analyzer (Picarro G-2401) and measured the O_2 mixing ratios

595   at the corresponding heights. Similar to the CO_2 measurements, O_2 was also measured for

three minutes at each height. During this period, we have evaluated the two features (isotopic mode and concentration mode) of the CRDS analyzer. In the isotopic mode, the CRDS measures the $\delta^{18}O$ values as well as the O_2 concentration while in concentration mode only the latter was measured.

During the tests conducted at this tower site, we first evaluated the two operational modes (concentration vs isotopic modes) of the CRDS analyzer. Ambient air measurements on isotopic mode over a 4-days period showed a strong variability in the measured oxygen mixing ratios and it was not possible to distinguish the variability in the O_2 mixing ratios among the five height levels. The calculated 1-minute standard error for ambient air measurements was as high as 10 ppm while a standard error of less than 1 ppm was determined from similar measurements in the concentration mode. Additionally, comparing the O_2 values between the two modes, frequent short time variation in ambient air O_2 ($\sim$ 200 ppm) was observed in the isotope mode measurements while the variation in the concentration mode is significantly smaller ($\sim$ 30 ppm). This precision degradation is due to the weaker ^{16}O oxygen line used for the isotopic mode, and the fact that far more ring-downs are collected on the rare isotopologue in isotopic mode Hence, we have conducted the remaining test measurements in concentration mode.

As this tower has five sampling height levels, we first followed three minutes of switching per inlet level, which enables four measurements per hour at a given level. However, we noticed hardly any difference among the different levels due to strong short term variability in O_2 mixing ratios between the consecutive heights. Hence, we switched to a longer sampling period of six-minutes per height. Figure 17 shows the diurnal CO_2 and O_2 variations at the lowest (12 m) and highest (212.5 m) sampling heights of the tower. These two heights were selected simply to better illustrate the difference in the mixing ratios. The

620   CO_2 mixing ratios on the top panel show higher values at the 12 m inlet than the highest level

621   most of the day due to its closeness to sources except during the afternoon (11:00 - 17:00

622   UTC) when both levels show similar but decreasing CO_2 mixing ratios. This is due to

623   presence of a well-mixed planetary boundary layer (PBL) (Satar et al., 2016). The lag in CO_2

624   peak between the two height levels by about two hours indicates the duration for uniform

625   vertical mixing along the tower during winter 2017. The opposite variability patterns are also

626   clearly visible in the O_2 mixing ratios shown in the lower panel with a clear distinction

627   between the two height levels during early in the morning and in the evening while similar O_2

628   values were observed in the afternoon. These opposing profiles are expected as CO_2 and O_2

629   are linearly coupled with a mean oxidation ratio of -1.1 ± 0.05 (Severinghaus, 1995) for land-

630   biospheric processes (photosynthesis and respiration) and -1.44 ± 0.03 for fossil fuel burning

631   (Keeling, 1988b).

632   Table 2 shows the oxidation ratios derived as the slopes of the linear regression

633   between CO_2 and O_2 mixing ratios at the different height levels measured on 25 February

634   2017. Accordingly, height dependent slopes were observed with a slope of -0.98 ± 0.06 at the

635   lowest level, close to the biological processes induced slope but slightly lower than its mean

636   value. For the highest level, we calculated a slope of -1.60 ± 0.07 a value close to fossil fuel

637   combustion oxidation ratio. Note that depending on fossil fuel type the oxidation ratio can

638   range between -1.17 and -1.95 for coal and natural gas, respectively (Keeling, 1988b). While

639   the slopes derived for the two other levels (44.6 m and 131.6 m) show similar values between

640   the highest and lowest height levels, possibly from mixed sources, the middle level showed a

641   slightly higher slope than these two levels but still in the large range between the lowest and

642   highest inlet heights.

643   3.4. Evaluation of the $\delta^{18}O$ measurements

644   To further evaluate the analyzer's performance in measuring stable oxygen isotopes,

645   we conducted ambient air isotopic composition measurements as well as analyzed a standard

646   gas without CO_2 which has a known $\delta^{18}O$ value. The choice of this CO_2-free air standard gas

647   is twofold: one it has a known $\delta^{18}O$ value and second as it has no interference from possible

648   CO_2 absorption band overlap. For this test three 0.5 L glass flasks were preconditioned and

649   filled with this standard gas to ambient pressure. These flasks were attached before or after

650   the water trap (Fig. 11) and measured similar to ambient air measurements. These

651   measurements were then compared with $\delta(^{34}O/^{32}O)$ values obtained by parallel measurements

652   using our IRMS.

653   Figure 18 shows the $\delta^{18}O$ values of ambient air from the roof top with three

654   consecutive measurements of glass flasks filled with CO_2-free air in-between followed by a

655   fourth flask filled with breath air. An excellent agreement was observed for measurements

656   from both instruments for the three flasks filled with a standard gas. However, the fourth flask

657   with breath air showed a signal opposite to the measurements by the IRMS. As breath air

658   contains large amount of water and CO_2 in addition to O_2, which can possibly interfere with

659   the CRDS analyzer measurements, we have removed H_2O and CO_2 by using a cryogenic trap

660   (-130 °C) and in an additional experiment using Schütze reagent to remove both CO and CO_2.

661   However, we have not observed any improvement towards an agreement with the IRMS

662   measurements. Therefore, any other gas component in the breath air must be relevant for the

663   interference. Based on the absorption lines in the spectral range of the instrument (7878 cm^{-1})

664   retrieved from HITRAN database, we expect interference either from carbon monoxide (now

665   excluded by the tests) or methane or VOCs including acetone, ethanol, methanol or isoprenes,

666   all of which have been measured in breath air (Gao et al., 2017; Gottlieb et al., 2017; Mckay

667   et al., 1985; Ryter and Choi, 2013; Wolf et al., 2017). Further investigations have to shed light

668 on these interferences in order to take corresponding action to surpass these shortcomings in

669 the isotope analysis based on cavity ring-down spectroscopy.

4. Conclusions

671   We have thoroughly evaluated the performance of a new CRDS analyzer which

672 measures O_2 mixing ratios and isotopic composition combining laboratory and field tests.

673 Even if a drift in the analyzer was observed at the beginning of this study, which can be easily

674 corrected by calibration, the recent analyzers built by the manufacturer did not show such

675 instrumental drift. However, prior tests are recommended to see the analyzer's stability.

676   The T-split tests for the current measurement setup based on the measurements of two

677 standard gases showed a difference within the measurement uncertainty. However, this effect

678 may become significant while applying larger splitting ratios and we recommend conducting

679 further experiments to accurately quantify this influence for larger splitting ratios.

680   We have observed a strong influence of dilution in the measured O_2 values during the

681 presence of high CO_2 mixing ratios. Even if such an influence may not be critical for the

682 present study, such an effect might be significant in other studies where higher CO_2 mixing

683 ratios might be present and we recommend following a correction strategy based on parallel

684 CO_2 measurements. This also applies for more accurate analysis.

685   The water correction applied by the instrument's in-built function seems to sufficiently

686 correct for the water vapor influence. However, a larger variability of the difference was

687 observed between the CRDS analyzer and the Paramagnetic cell when dried samples were

688 used in both systems. This can possibly be due to an overcorrection by the water correction

689 function of the CRDS analyzer when dried samples were used. This is particularly true for the

690 very low water vapor range (< 100 ppm). We believe that it is important to further investigate

691 this issue and identify an improved water correction strategy.

692   Based on the analysis of O_2 mixing ratios in the concentration and isotopic modes, we

693   have observed a significant decrease in precision (about ten-fold) in the latter measurement

694   mode. The measured $\delta^{18}O$ values for the standard air by the CRDS analyzer are in excellent

695   agreement with the IRMS values. However, such measurements for a breath air showed a

696   contrasting signal, possibly due to interference from other gases such as CH_4. Hence, we

697   recommend further investigation on such possible contaminants and how to possibly remove

698   them while conducting ambient air measurements. However, we believe that this analyzer can

699   be used for tracer experiments where artificially enriched isotopes are used to study biological

700   processes such as photosynthesis in plants using isotopically labelled CO_2 and H_2O.

701   **Acknowledgement**

702   We would like to thank ICOS-RI and the Swiss National Science Foundation (SNF) for

703   funding ICOS-CH (20FI21_148994, 20FI21_148992). We are also grateful to the

704   International Foundation High Alpine Research Stations Jungfraujoch and Gornergrat. The

705   measurement system at the Beromünster tower was built and maintained by the CarboCount-

706   CH (CRSII2_136273) and IsoCEP (200020_172550) projects both funded by SNF.

707

708

709

710

711

712

713

714

715

716 List of Tables

717 Table 1. Assigned mixing ratios of standard gases used in this study and their corresponding

718 values measured by the NDIR, CRDS and IRMS at the University of Bern. [1]The assigned

719 values are based on measurements from different institutions (University of Bern (UB),

720 Scripps or NOAA, see column cylinder name). [2]Measurements are on the Bern scale for CO_2

721 and O_2. The Bern scale is shifted by +550 per meg. [3]Values on the Scripps scale.

722

Cylinder name	Assigned CO_2 (ppm) [1]	Assigned O_2 (per meg) [1]	CO_2-IRMS (ppm) [2]	CO_2-NDIR (ppm) [2]	O_2-IRMS (per meg) [2]	O_2-Paramagnetic (per meg) [2]	O_2-CRDS (per meg) [2]
ST-1 LUX3576-UB	427.47	-1026	427.47	427.59	-1026	-1070	-1057
ST-2 LK922131-UB	368.09	599	368.09	367.82	599	560	590
ST-3 CA07045-Scripps	382.303	-271.6	382.50	381.99	278 (-272.2)[3]	302	281
ST-4 CA07043-Scripps	390.528	-476.4	390.69	390.15	71 (-479.5)[3]	66	63
ST-5 CA07047-Scripps	374.480	-807.7	374.70	374.17	-253 (-803.3)[3]	-212	-233
ST-6 CA04556-NOAA	192.44	-3410	191.21	191.64	-3410	-2905	-3013
ST-7 CA06943-	2699.45	-		2612.80	-	-2691	-3369

NOAA						
ST-8 LK76852-UB	411.49	37794	411.49	406.25	37794	34513	36017

Table 2. The CO_2 and O_2 correlation coefficients at the different height levels derived using the least square fit and the correlation coefficients (r^2). Uncertainties are calculated as standard error of the slope.

Height	Oxidation Ratios (O_2:CO_2)
12.5 m	-0.98 ± 0.06 (0.48)
44.6 m	-1.29 ± 0.07 (0.50)
71.5 m	-1.49 ± 0.08 (0.47)
131.6 m	-1.23 ± 0.05 (0.55)
212.5 m	-1.60 ± 0.07 (0.61)
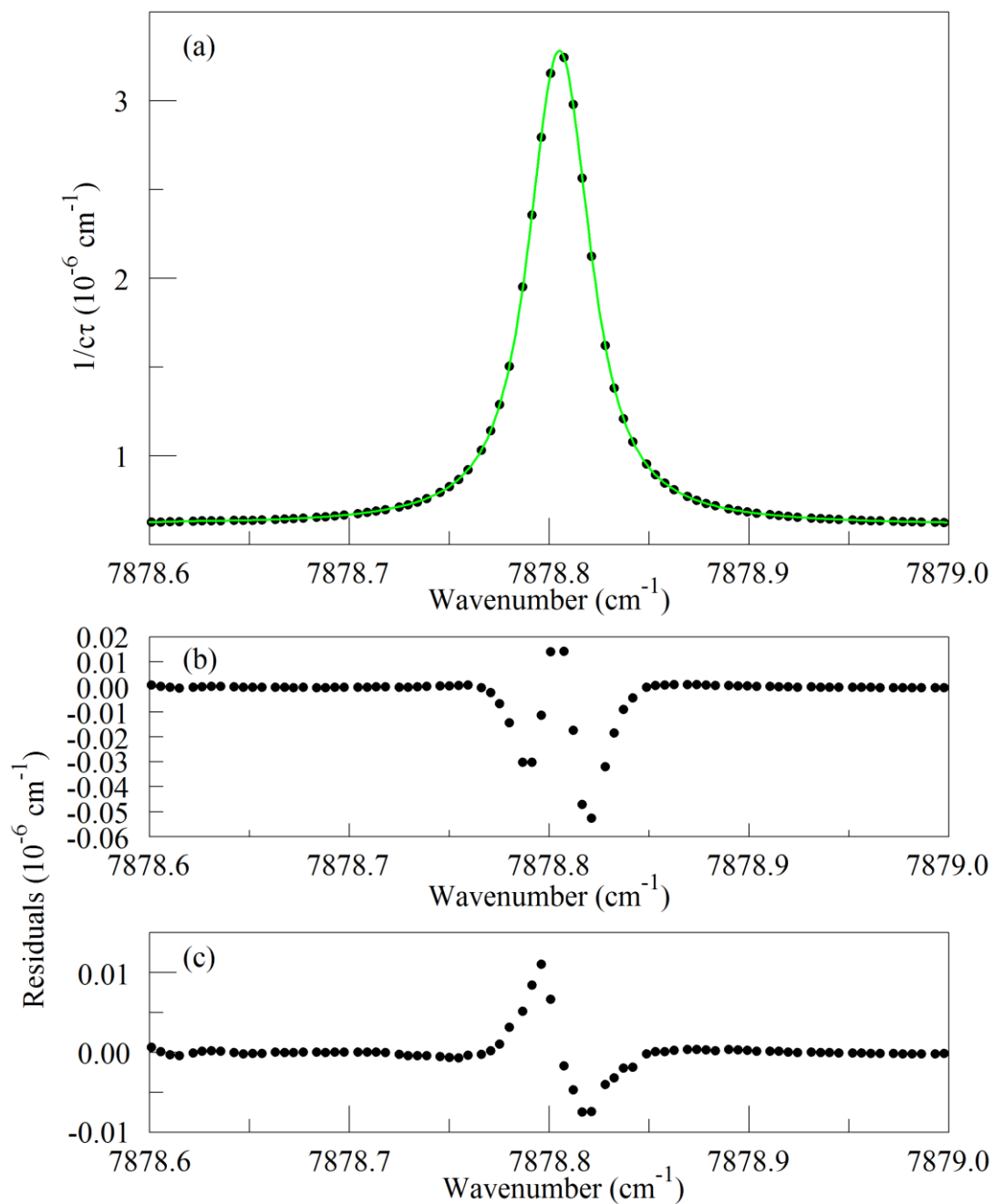
737

738   Figure 1. The top panel (a) shows the raw data (points) and the best-fit Galatry function (solid

739   line). Residuals of the Voigt fit are shown in panel (b) and residuals of the Galatry fit are

740   shown in panel (c).

741

742
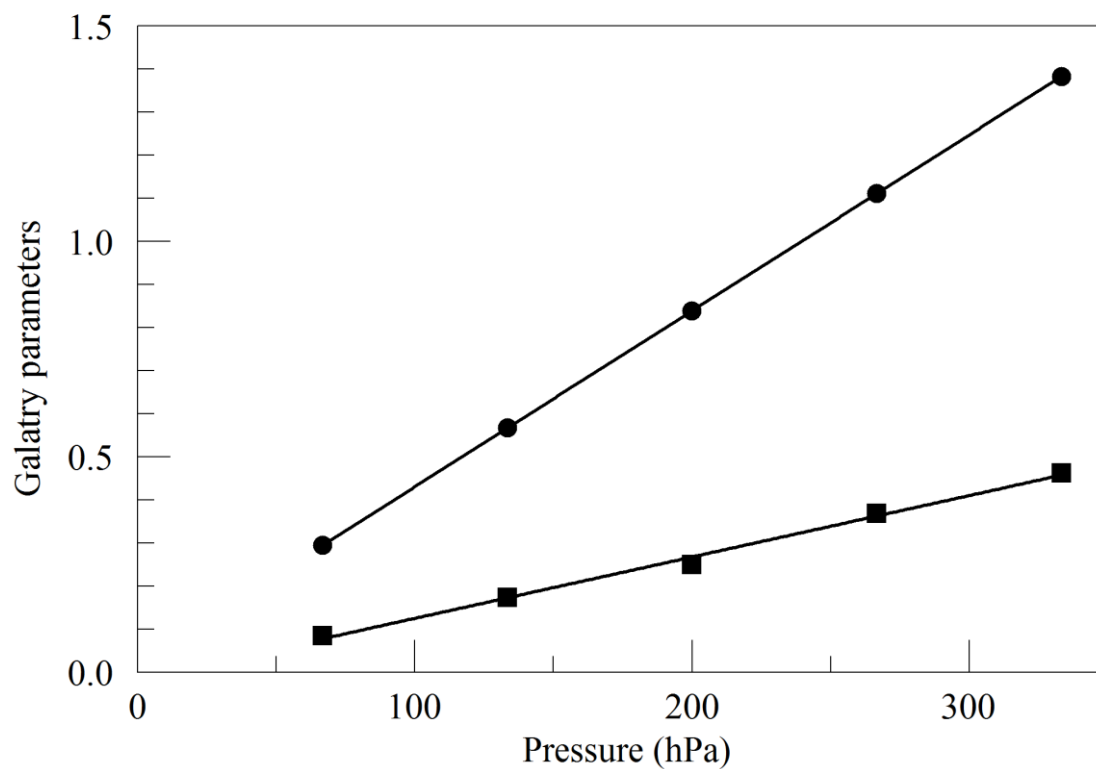
743

744   Figure 2. Best-fit values for the Galatry parameters of the Q13Q13 line of O_2, as a function of

745   pressure. The line broadening parameter y is represented by circles and the line narrowing

746   parameter z by squares. The solid lines are linear fits to the measurements. The best-fit offset

747   and slope are 0.0227 and 0.004082 hPa^{-1} for y, and -0.0169 and 0.001424 hPa^{-1} for z.
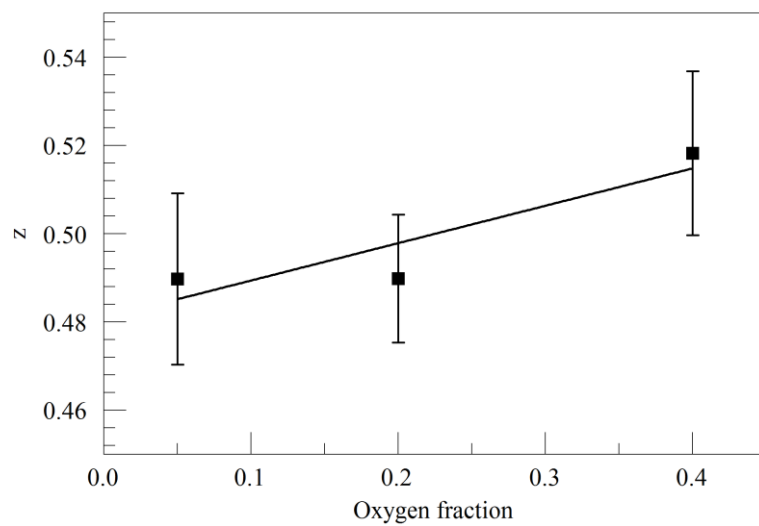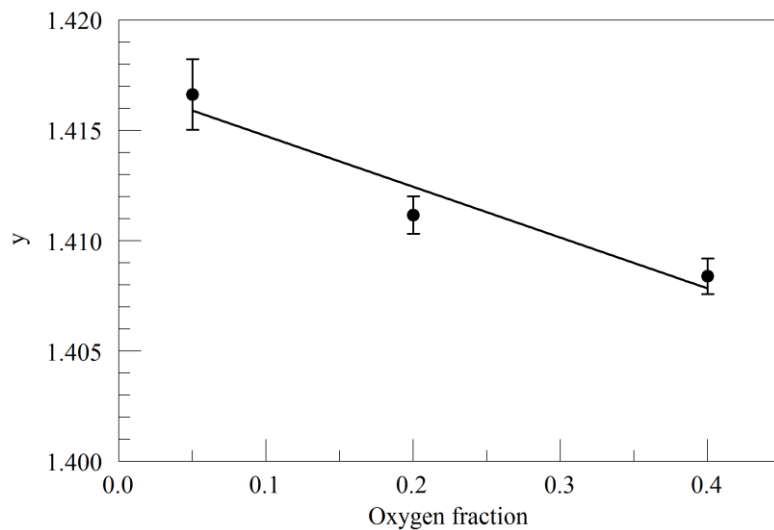
748

749   Figure 3. Galatry parameters of the Q13Q13 line of O_2 at 340 hPa and 45° C as a function of

750   O_2 mole fraction in binary O_2 - N_2 mixtures. The linear fits to the data are y = 1.417 – 0.023 x

751   f_{O2} and z = 0.481 + 0.085 x f_{O2}.
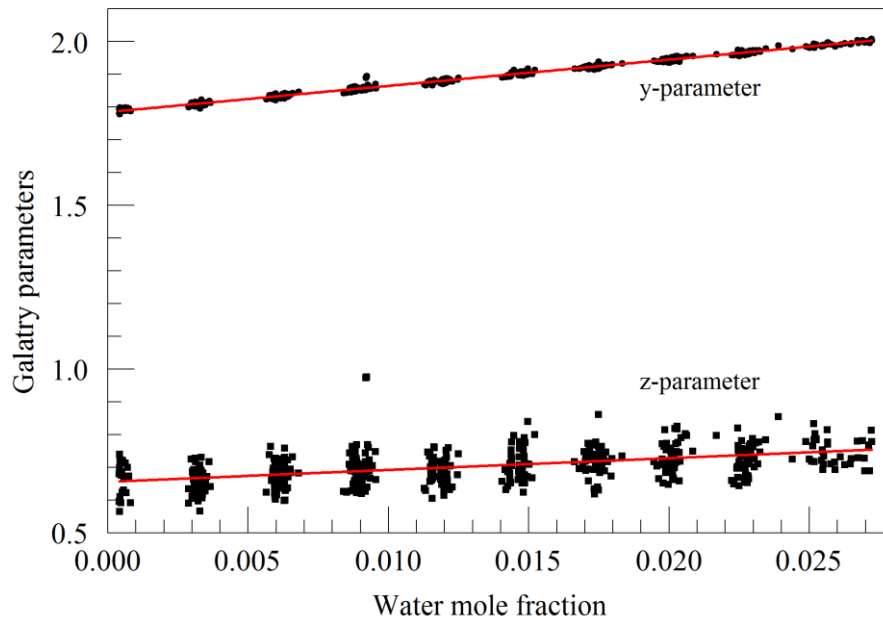
752

753 Figure 4. Galatry parameters of the 7816.75210 cm^{-1} water line in air at 340 hPa and 45° C as

754 a function of water mole fraction. Black points are from measurements and red lines are

755 linear fits: $y = 1.7846 + 8.01 \times f_{H2O}$ and $z = 0.656 + 3.60 \times f_{H2O}$.

756

757

758
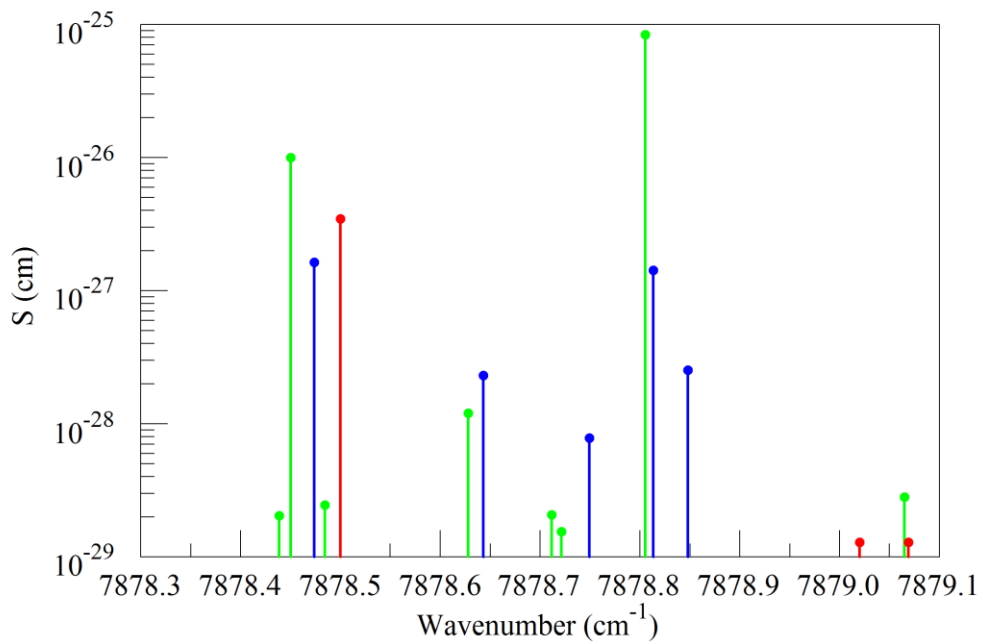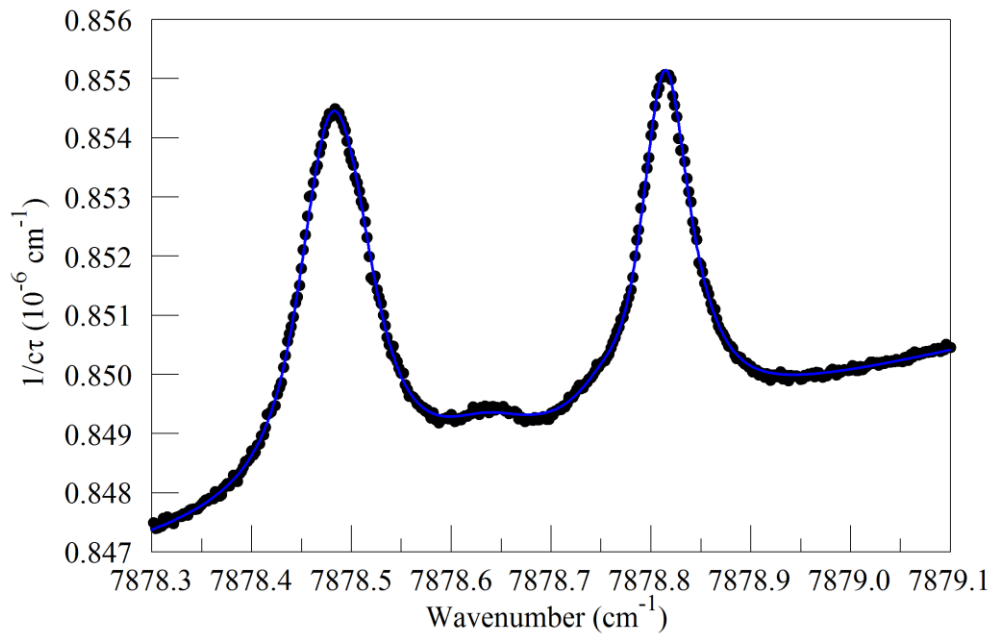
759

760   Figure 5. Upper panel: spectrum of water in nitrogen (points) and fit to Voigt model (blue

761   curve). Lower panel: Oxygen (green), normal water (blue), and deuterated water (red) lines

762   in the 2016 Hitran data base.

763

764
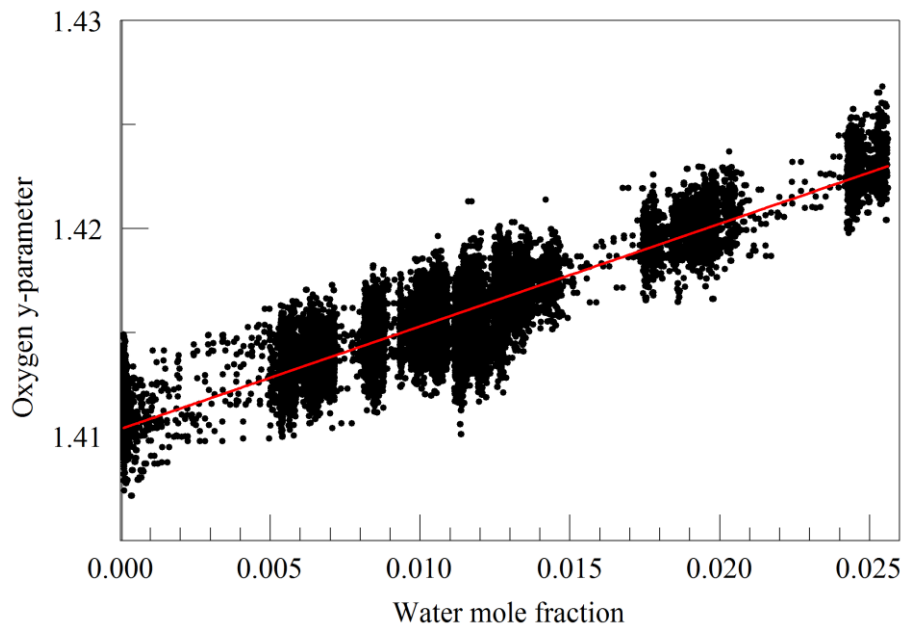
765

766   Figure 6.   Galatry collisional broadening parameter of the oxygen Q13Q13 line at 340 hPa

767   and 45° C versus water mole fraction. Black points are from measurements and the red line is

768   a linear fit: $y = 1.4109 + 0.467\ f_{H2O}$.

769

770

771
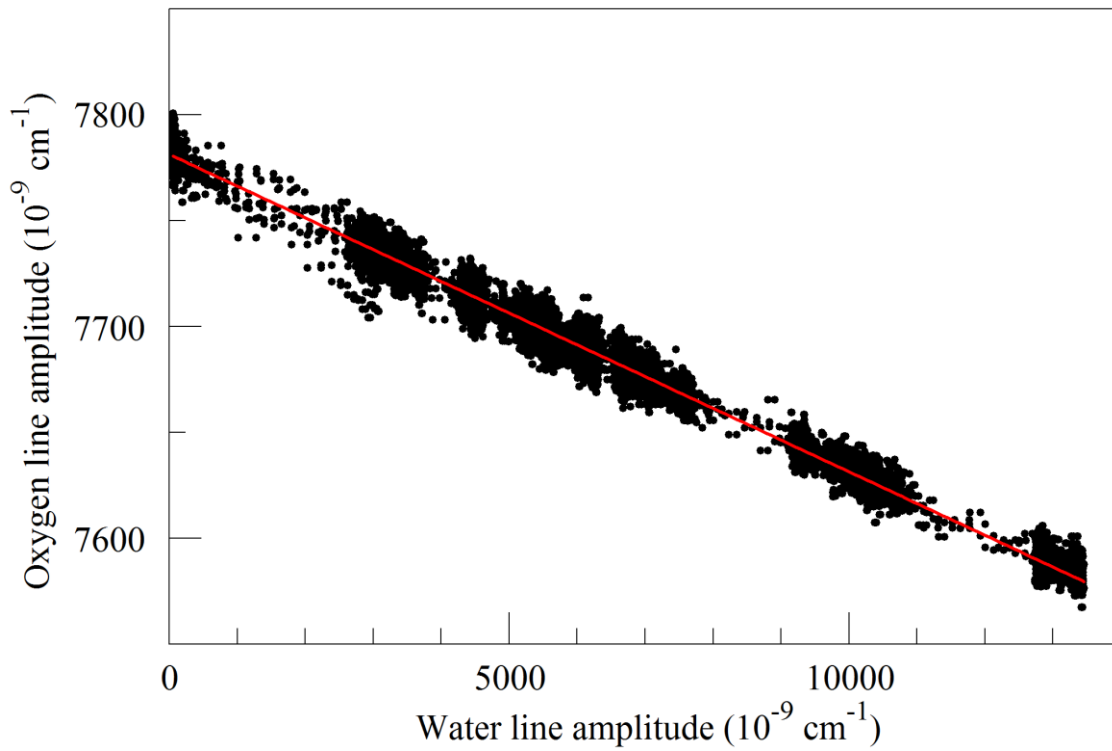
772

773 Figure 7. Measured absorption line amplitudes for oxygen and water vapor for water vapor

774 mixing ratios ranging from nearly 0 to 0.025. Black points are from measurements and the

775 red line is a linear fit: with intercept 7.78001 x 10^{-6} cm^{-1} and slope -0.014807.

776

777

778

779

780

781

782
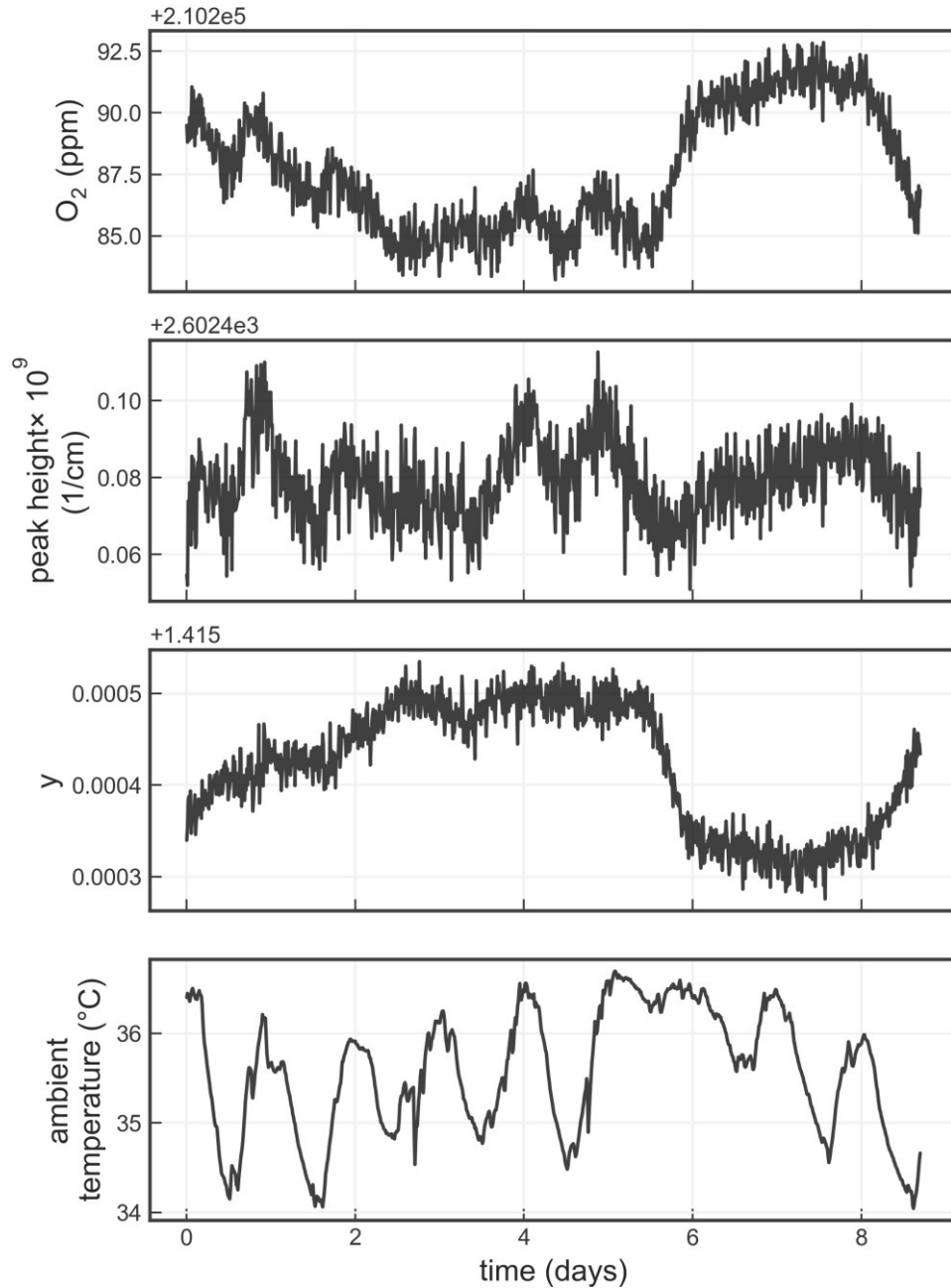
Figure 8. Time series from a measurement of a single tank over about a week. The four panels

show the water-corrected oxygen concentration, the absorption peak loss minus the baseline

loss, the measured Lorentzian broadening factor, and the ambient temperature (measured in

the instrument housing), respectively. A windowed average of 300 seconds was applied to all

four data sets.
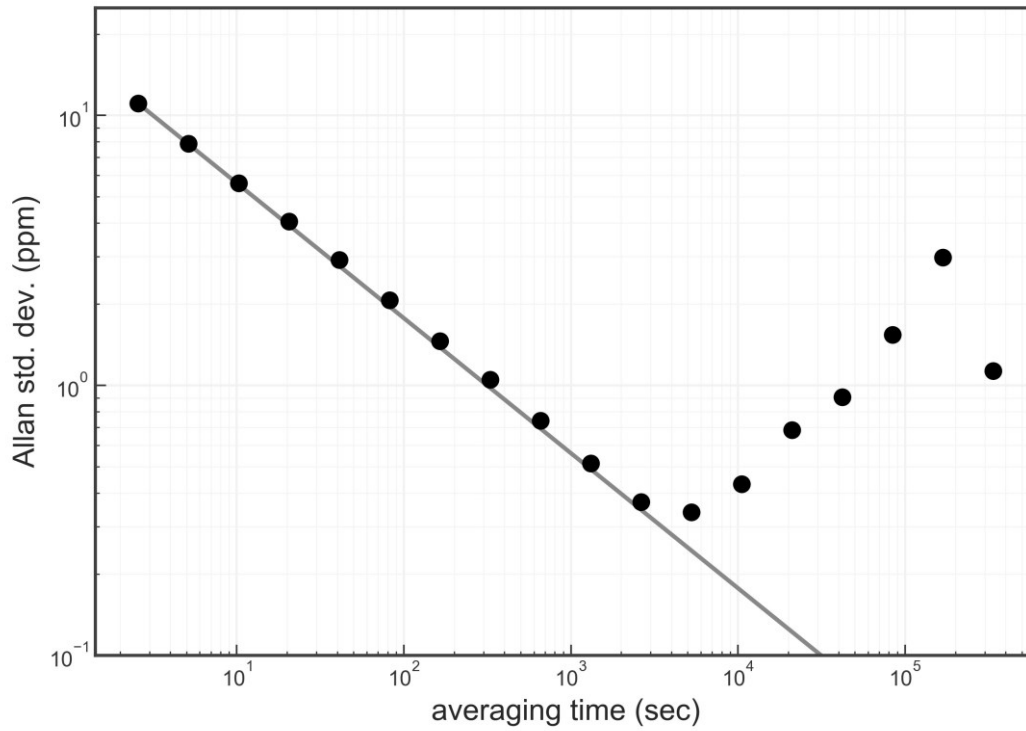
788

789 Figure 9. Precision of O_2 mole fraction measured from a tank of synthetic air. Filled circles

790 are measurements and the line shows the ideal $\tau^{-1/2}$ dependence.

791

792

793

794

795
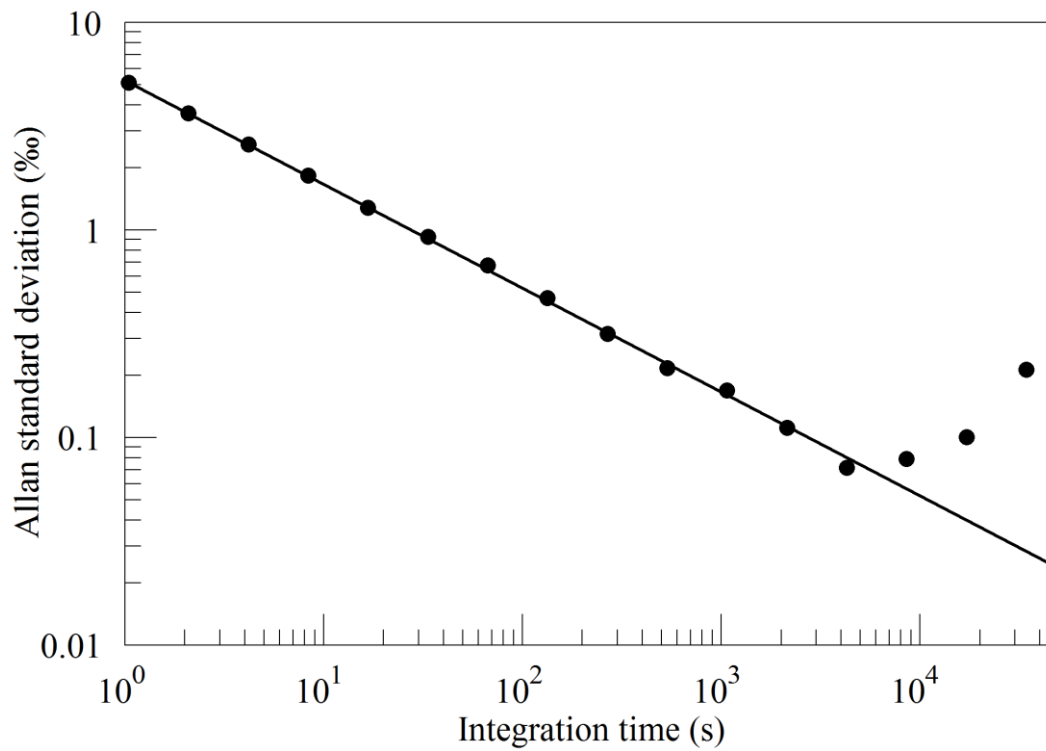
Figure 10. Precision of $\delta(^{18}O)$ measured from a tank of synthetic air. Filled circles are measurements and the line shows the ideal $\tau^{-1/2}$ dependence.
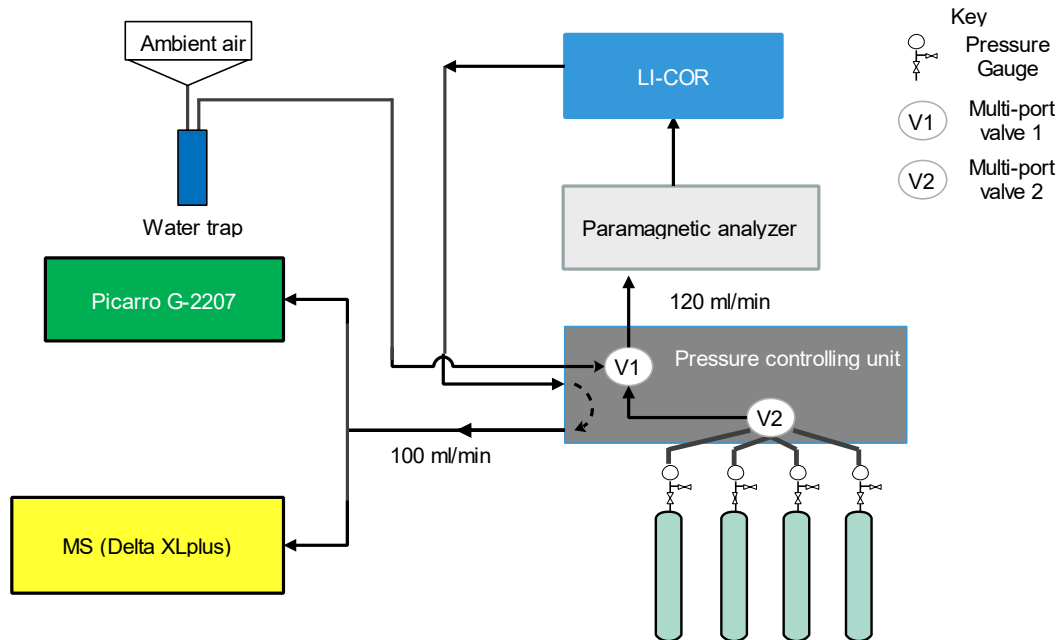
807

808 Figure 11. Schematics of the measurement system used to compare the Picarro analyzer with

809 the Mass Spectrometer at Bern.

810

811

812

813

814

815

816

817

818
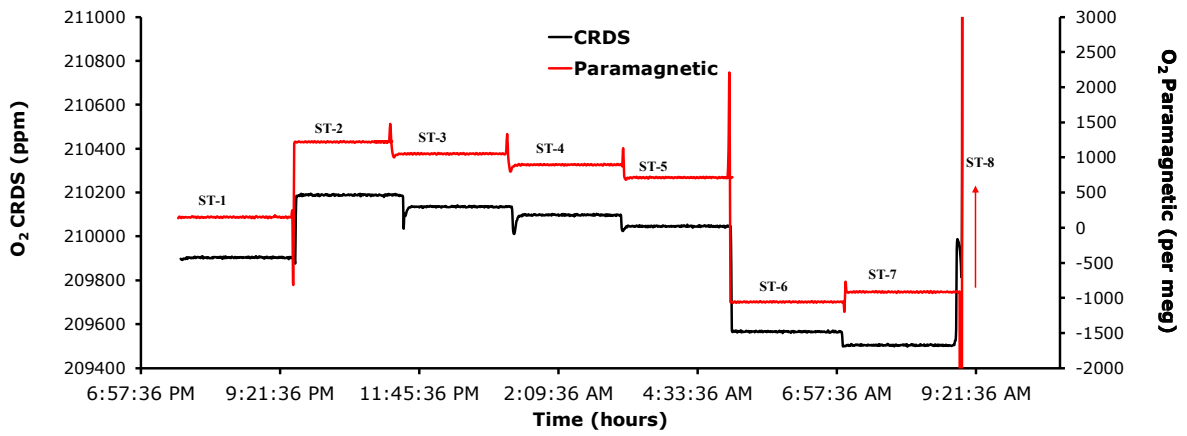
819

820 Figure 12. Comparison of oxygen mixing ratios for the seven standard gases measured using

821 the CRDS analyzer (black) and the Paramagnetic sensors (red).

822

823

824

825

826

827

828

829

830

831

832

833

834

835

836

837
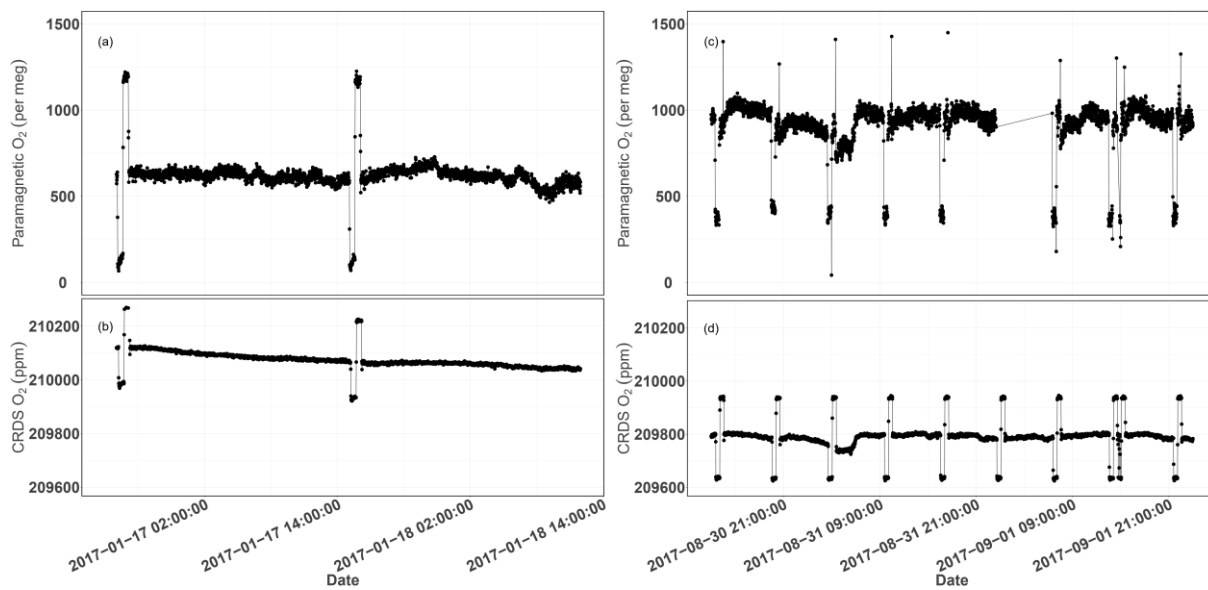
838

839   Figure 13. Parallel ambient air measurements by the Paramagnetic and CRDS analyzers at the

840   beginning of the testing period (Panels a & b, January 2017) and the second phase of testing

841   (Panels c & d, September 2017). The spikes are measurements from the two standard gases

842   bracketing the ambient air values.

843

844

845

846

847

848

849

850

851

852

853

854
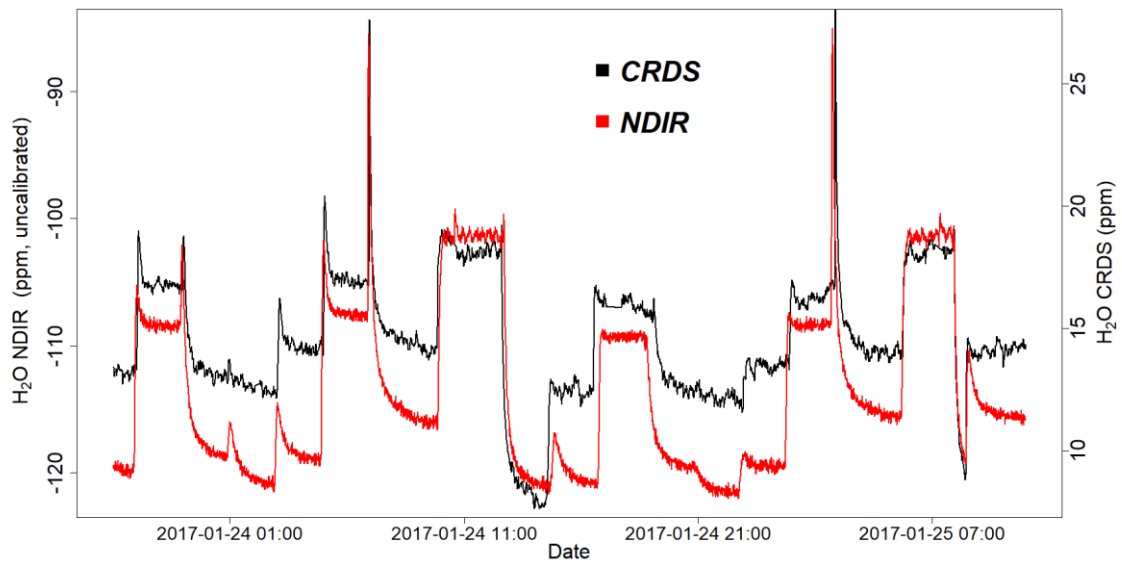
855

856   Figure 14. Parallel water vapor measurements for a dried ambient air by both the NDIR and

857   CRDS analyzers. Note that the water values from the NDIR analyzer are not calibrated.

858

859

860

861

862

863

864

865

866

867

868

869

870
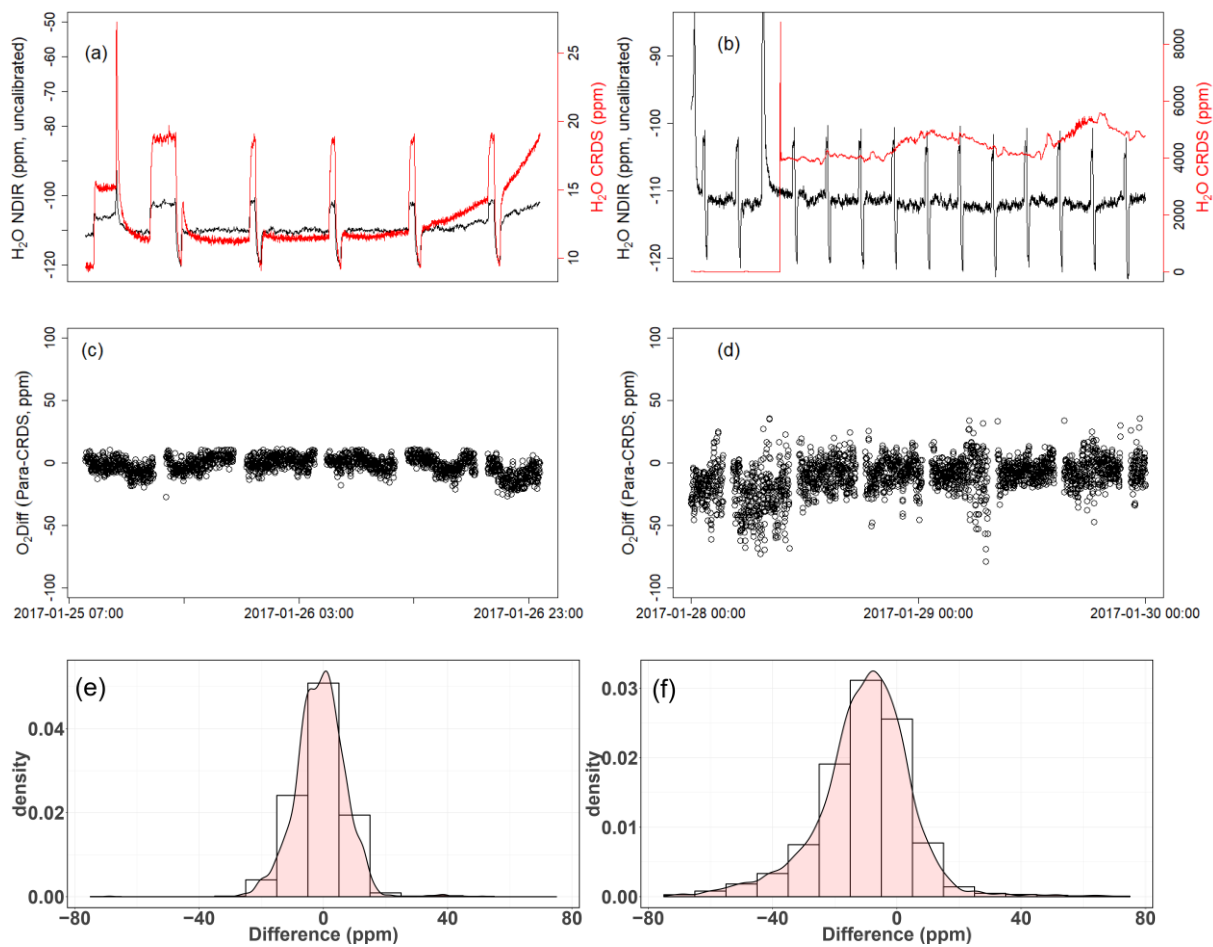
871

872

873 Figure 15. Results of water correction tests. Water measurements of the NDIR (left scale) for

874 dry conditions (a,b) and the CRDS analyzer (right scale) for dry (a) and wet (b) conditions.

875 The difference in oxygen measurements between the Paramagnetic and the CRDS instrument

876 using the built-in water correction for the CRDS values under dry (c) and wet (d) conditions.

877 Panels (e) and (f) show the population density functions.

878

879

880

881

882
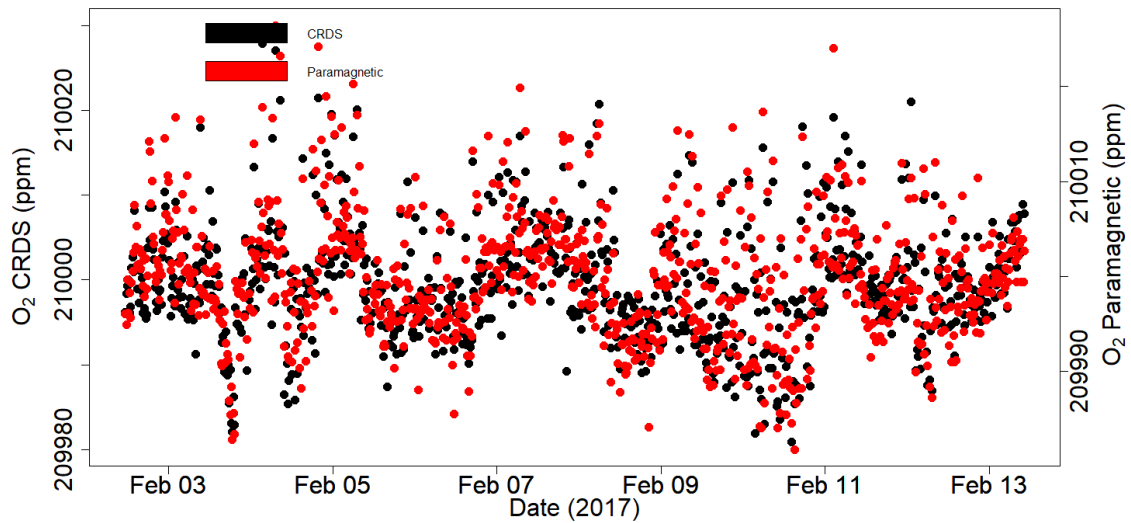
883
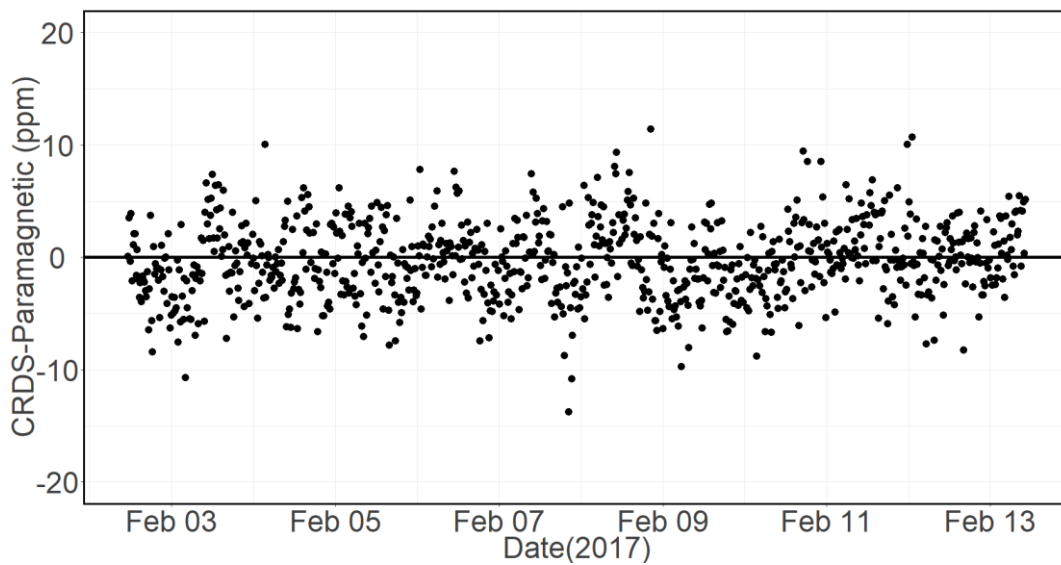
884

885   Figure 16. Calibrated ambient air oxygen measurements (1-minute average) at the

886   Jungfraujoch site using the CRDS and Paramagnetic analyzers both in ppm units (a) and the

887   absolute difference between the two measurements in ppm (b) by matching time stamps

888

889

890

891

892
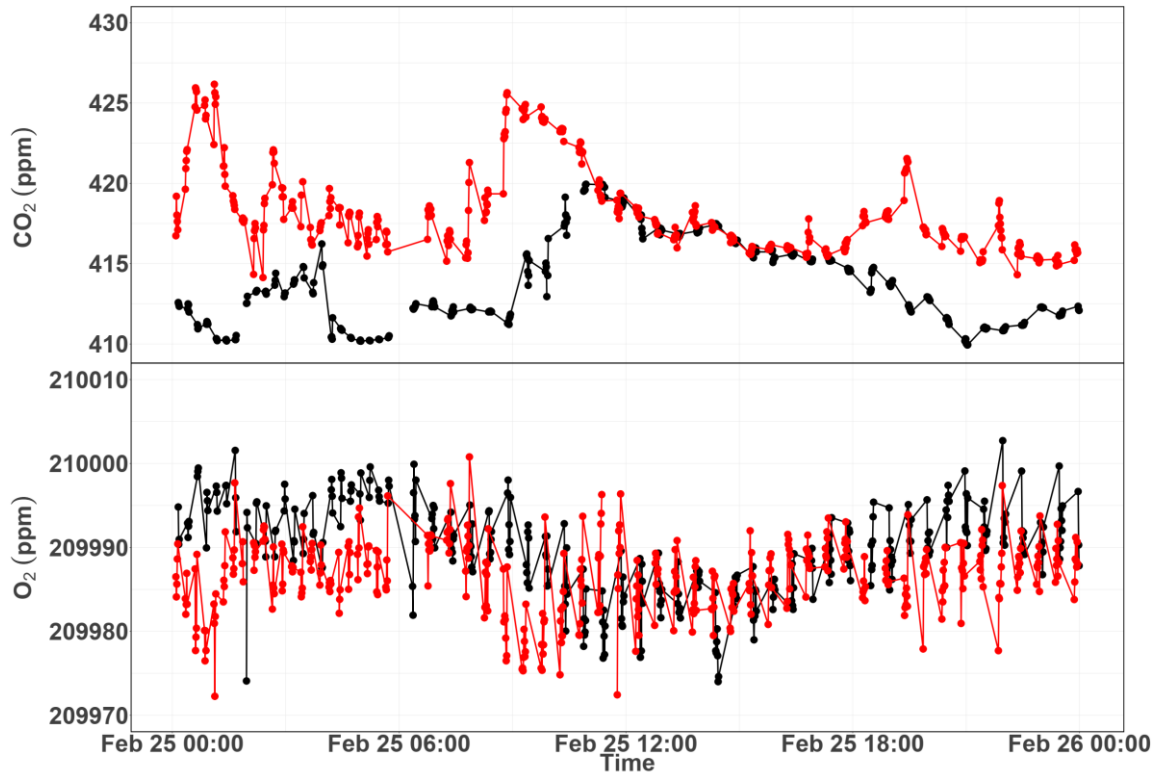
893

894   Figure 17. Diurnal variations of CO_2 (top) and O_2 (bottom) measurements from the 12 m (red)

895   and the 212.5 m (black) height levels at Beromünster tower.

896

897

898

899

900

901

902

903

904

905
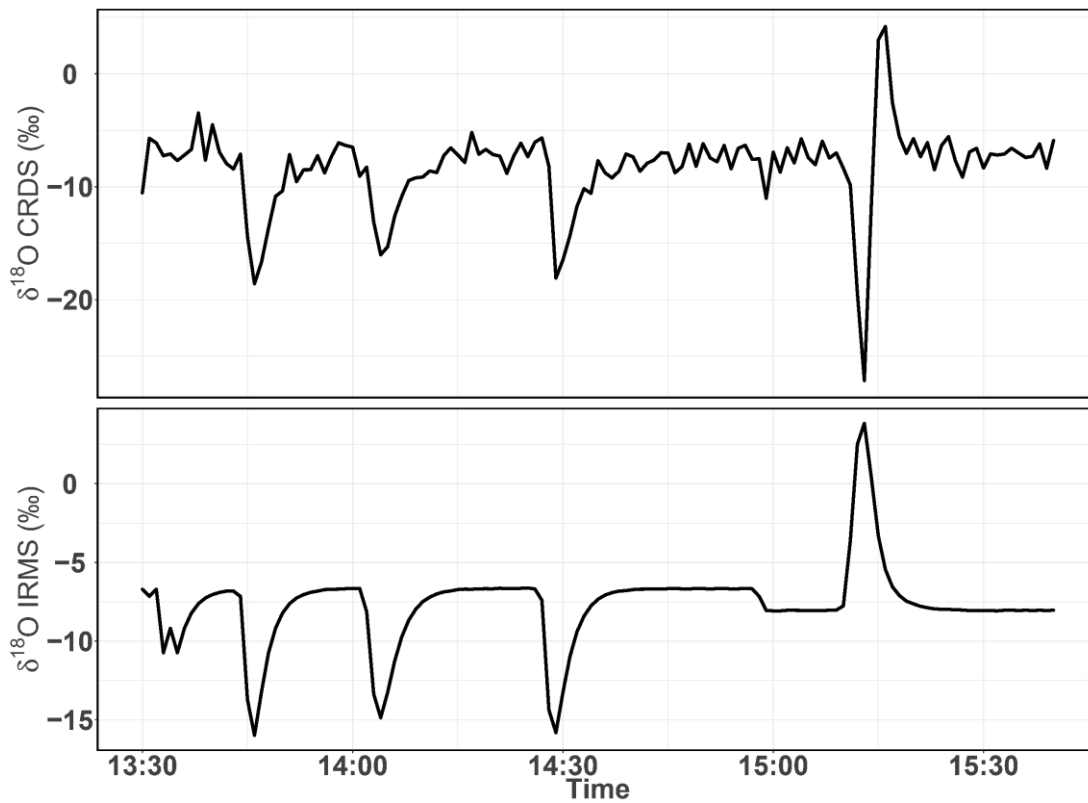
Figure 18. Consecutive $\delta^{18}O$ measurements of a standard gas (CO_2-free air) filled into three flasks followed by measurement of breath air using the CRDS analyzer (top) and IRMS (bottom). These measurements were carried out in the middle of ambient air measurements.

Appendix A.
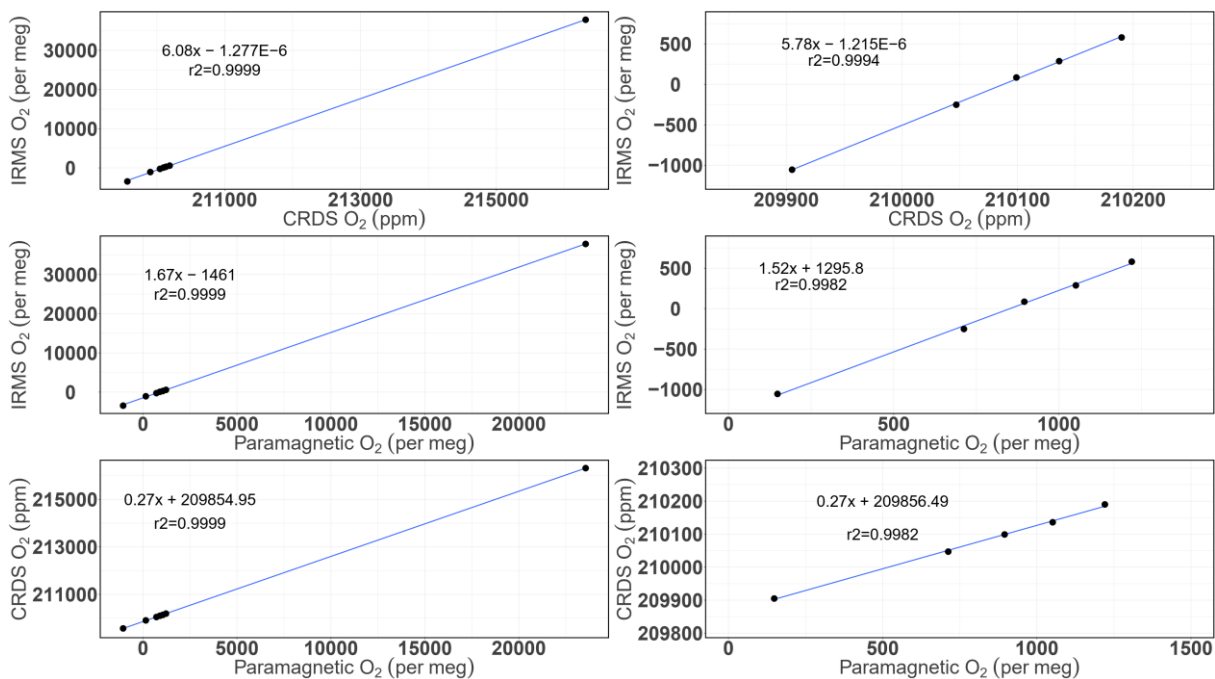
Figure A.1. Correlations between the O_2 mixing ratios measured by the CRDS and Paramagnetic analyzers with the mass spectrometric measurements (uncalibrated values). The left panels are for all the cylinders measured (standards 1 to 8) while the right ones are after selecting standards 1-5.

References

935

936 Battle, M., Bender, M. L., Tans, P. P., White, J. W. C., Ellis, J. T., Conway, T., and Francey, R. J.: Global

937 carbon sinks and their variability inferred from atmospheric O-2 and delta C-13, Science, 287, 2467-

938 2470, 2000.

939 Bender, M. L., Tans, P. P., Ellis, J. T., Orchardo, J., and Habfast, K.: A High-Precision Isotope Ratio

940 Mass-Spectrometry Method for Measuring the O-2 N-2 Ratio of Air, Geochim Cosmochim Ac, 58,

941 4751-4758, 1994.

942 Berhanu, T. A., Satar, E., Schanda, R., Nyfeler, P., Moret, H., Brunner, D., Oney, B., and Leuenberger,

943 M.: Measurements of greenhouse gases at Beromünster tall tower station in Switzerland, Atmos.

944 Meas. Tech. , 9, 2016.

945 Berhanu, T. A., Szidat, S., Brunner, D., Satar, E., Schanda, R., Nyfeler, P., Battaglia, M., Steinbacher,

946 M., Hammer, S., and Leuenberger, M.: Estimation of the fossil-fuel component in atmospheric CO2

947 based on radiocarbon measurements at the Beromünster tall tower, Switzerland, Atmos. Chem.

948 Phys. Discuss., 2017, 1-33, 2017.

949 Crosson, E. R. J. A. P. B.: A cavity ring-down analyzer for measuring atmospheric levels of methane,

950 carbon dioxide, and water vapor, 92, 403-408, 2008.

951 Filges, A., Gerbig, C., Rella, C. W., Hoffnagle, J., Smit, H., Krämer, M., Spelten, N., Rolf, C., Bozóki, Z.,

952 Buchholz, B., and Ebert, V.: Evaluation of the IAGOS-Core GHG Package H2O measurements during

953 the DENCHAR airborne inter-comparison campaign in 2011, Atmos. Meas. Tech., 11, 5279–5297,

954 2018, https://doi.org/10.5194/amt-11-5279-2018. Gao, F., Zhang, X., Zhang, X., Wang, M., and Wang,

955 P.: Virtual electronic nose with diagnosis model for the detection of hydrogen and methane in breath

956 from gastrointestinal bacteria, 28-31 May 2017 2017, 1-3.

957 Gordon, E., Rothman, S., Hill, C., Kochanov, V., Tan, Y., Bernath, P., Birk, M., Boudon, V., Campargue,

958 A., Chance, K., Drouin, J., Flaud, J., Gamache, R. R., Hodges, J., Jacquemart, D., Perevalov, I., Perrin, A.,

959 Shine, P., Smith, M., Tennyson, J., Toon, G., Tran, H., Tyuterev, G., Barbe, A., Császár, G., Devi, M.,

960   Furtenbacher, T., Harrison, J., Hartmann, J., Jolly, A., Johnson, J., Karman, T., Kleiner, I., Kyuberis, A.

961   A., Loos, J., Lyulin, M., Massie, S., Mikhailenko, S., Moazzen-Ahmadi, N., Muller, S., Naumenko, O. V.,

962   Nikitin, A. V., Polyansky, O. L., Rey, M., Rotger, M., Sharpe, S., Sung, K., Starikova, E., Tashkun, S.,

963   Auwera, J., Wagner, G., Wilzewski, J., Wcisło, P., Yu, S., and Zak, E. J.: The HITRAN2016 molecular

964   spectroscopic database, 203, 3 - 69, 2017.

965   Goto, D., Morimoto, S., Ishidoya, S., Aoki, S., and Nakazawa, T.: Terrestrial biospheric and oceanic

966   CO_2 uptake estimated from long-term measurements of atmospheric CO_2 mole fraction, δ13C and

967   δ(O2/N2) at Ny-Ålesund, Svalbard, Journal of Geophysical Research: Biogeosciences, doi:

968   10.1002/2017JG003845, 2017. n/a-n/a, 2017.

969   Gottlieb, K., Le, C. X., Wacher, V., Sliman, J., Cruz, C., Porter, T., and Carter, S.: Selection of a cut-off

970   for high- and low-methane producers using a spot-methane breath test: results from a large north

971   American dataset of hydrogen, methane and carbon dioxide measurements in breath, Gastroenterol

972   Rep, 5, 193-199, 2017.

973   Hartmann, J.-M., Boulet, C., and Robert, D.: Collisional Effects on Molecular Spectra, Elsevier Science,

974   2008.

975   Henne, S., Brunner, D., Folini, D., Solberg, S., Klausen, J., and Buchmann, B.: Assessment of

976   parameters describing representativeness of air quality in-situ measurement sites, Atmos. Chem.

977   Phys., 10, 3561-3581, 2010.

978   Hodges, J. T., Layer, H. P., Miller, W. W., and Scace, G. E.: Frequency-stabilized single-mode cavity

979   ring-down apparatus for high-resolution absorption spectroscopy, 75, 849-863, 2004.

980   Keeling, R. F.: Development of an Interferometric Oxygen Analyzer for Precise Measurement of the

981   Atmospheric O2 Mole Fraction, UMI, 1988a.

982   Keeling, R. F.: Measuring correlations between atmospheric oxygen and carbon dioxide mole

983   fractions: A preliminary study in urban air, J Atmos Chem, 7, 153-176, 1988b.

984 Keeling, R. F. and Manning, A. C.: 5.15 - Studies of Recent Changes in Atmospheric O2 Content A2 -

985 Holland, Heinrich D. In: Treatise on Geochemistry (Second Edition), Turekian, K. K. (Ed.), Elsevier,

986 Oxford, 2014.

987 Keeling, R. F. and Shertz, S. R.: Seasonal and Interannual Variations in Atmospheric Oxygen and

988 Implications for the Global Carbon-Cycle, Nature, 358, 723-727, 1992.

989 Keeling, R. F., Stephens, B. B., Najjar, R. G., Doney, S. C., Archer, D., and Heimann, M.: Seasonal

990 variations in the atmospheric O-2/N-2 ratio in relation to the kinetics of air-sea gas exchange, Global

991 Biogeochem Cy, 12, 141-163, 1998.

992 Lamouroux, J., Sironneau, V., Hodges, J. T., and Hartmann, J. M.: Isolated line shapes of molecular

993 oxygen: Requantized classical molecular dynamics calculations versus measurements, Physical

994 Review A, 89, 042504, 2014.

995 Le Quéré, C., Andrew, R. M., Friedlingstein, P., Sitch, S., Pongratz, J., Manning, A. C., Korsbakken, J. I.,

996 Peters, G. P., Canadell, J. G., Jackson, R. B., Boden, T. A., Tans, P. P., Andrews, O. D., Arora, V. K.,

997 Bakker, D. C. E., Barbero, L., Becker, M., Betts, R. A., Bopp, L., Chevallier, F., Chini, L. P., Ciais, P.,

998 Cosca, C. E., Cross, J., Currie, K., Gasser, T., Harris, I., Hauck, J., Haverd, V., Houghton, R. A., Hunt, C.

999 W., Hurtt, G., Ilyina, T., Jain, A. K., Kato, E., Kautz, M., Keeling, R. F., Klein Goldewijk, K., Körtzinger, A.,

1000 Landschützer, P., Lefèvre, N., Lenton, A., Lienert, S., Lima, I., Lombardozzi, D., Metzl, N., Millero, F.,

1001 Monteiro, P. M. S., Munro, D. R., Nabel, J. E. M. S., Nakaoka, S. I., Nojiri, Y., Padín, X. A., Peregon, A.,

1002 Pfeil, B., Pierrot, D., Poulter, B., Rehder, G., Reimer, J., Rödenbeck, C., Schwinger, J., Séférian, R.,

1003 Skjelvan, I., Stocker, B. D., Tian, H., Tilbrook, B., van der Laan-Luijkx, I. T., van der Werf, G. R., van

1004 Heuven, S., Viovy, N., Vuichard, N., Walker, A. P., Watson, A. J., Wiltshire, A. J., Zaehle, S., and Zhu,

1005 D.: Global Carbon Budget 2017, Earth Syst. Sci. Data Discuss., 2017, 1-79, 2017.

1006 Machta, L. Hughes, E. Atmopsheric Oxygen in 1967 to 1970, Science, 168, 3939, 1582-1584, 1970.

1007   Manning, A.: Temporal variability of atmospheric oxygen from both continuos and measurements

1008   and a flask sampling network: tools for studying the global carbon cycle, Ph.D. Ph.D., University of

1009   California, San Diego, San Diego, Calofornia, USA, 2001.

1010   Manning, A. C. and Keeling, R. F.: Global oceanic and land biotic carbon sinks from the Scripps

1011   atmospheric oxygen flask sampling network, Tellus B, 58, 95-116, 2006.

1012   Manning, A. C., Keeling, R. F., and Severinghaus, J. P.: Precise atmospheric oxygen measurements

1013   with a paramagnetic oxygen analyzer, Global Biogeochem Cy, 13, 1107-1115, 1999.

1014   Marrero, T. R. and Mason, E. A.: Gaseous Diffusion Coefficients, Journal of Physical and Chemical

1015   Reference Data 1, 3, 1972.

1016   Martin, N. A., Ferracci, V., Cassidy, N., and Hoffnagle, J. A. J. A. P. B.: The application of a cavity ring-

1017   down spectrometer to measurements of ambient ammonia using traceable primary standard gas

1018   mixtures, 122, 219, 2016.

1019   Mckay, L. F., Eastwood, M. A., and Brydon, W. G.: Methane Excretion in Man - a Study of Breath,

1020   Flatus, and Feces, Gut, 26, 69-74, 1985.

1021   Nevison, C. D., Keeling, R. F., Kahru, M., Manizza, M., Mitchell, B. G., and Cassar, N.: Estimating net

1022   community production in the Southern Ocean based on atmospheric potential oxygen and satellite

1023   ocean color data, Global Biogeochem Cy, 26, 2012.

1024   Oney, B., Henne, S., Gruber, N., Leuenberger, M., Bamberger, I., Eugster, W., and Brunner, D.: The

1025   CarboCount CH sites: characterization of a dense greenhouse gas observation network, Atmos.

1026   Chem. Phys., 15, 11147-11164, 2015.

1027   Press, W. H., Teukolsky, S. A., Vetterling, W. T., and Flannery, B. P.: Numerical Recipes 3rd Edition:

1028   The Art of Scientific Computing, Cambridge Printing Press, Cambridge, England, 1986.

1029   Press, W. H., Teukolsky, S. A., Vetterling, W. T., and Flannery, B. P.: Numerical recipes in C: the art of

1030   scientific computing, Cambridge University Press, London, 1992.

1031   Ryter, S. W. and Choi, A. M. K.: Carbon monoxide in exhaled breath testing and therapeutics, J Breath

1032   Res, 7, 2013.

1033   Satar, E., Berhanu, T. A., Brunner, D., Henne, S., and Leuenberger, M.: Continuous CO2/CH4/CO

1034   measurements (2012–2014) at Beromünster tall tower station in Switzerland, Biogeosciences, 13,

1035   2623-2635, 2016.

1036   Schibig, M. F., Steinbacher, M., Buchmann, B., van der Laan-Luijkx, I. T., van der Laan, S., Ranjan, S.

1037   and Leuenberger, M. C,: Comparison of continuous in situ CO2 observations at Jungfraujoch using

1038   two different measurement techniques, Atmospheric Measurement Techniques

1039   , 8, 57-68, 10.5194/amt-8-57-2015, 2015.

1040   Severinghaus, J. P.: Studies of the terresterial O2 and carbon cycles in sand dune gases and in

1041   Biosphere Doctoral Ph.D., Columbia University, New York, USA, 1995.

1042   Steig, E. J., Gkinis, V., Schauer, A. J., Schoenemann, S. W., Samek, K., Hoffnagle, J., Dennis, K. J., and

1043   Tan, S. M.: Calibrated high-precision [17]O-excess measurements using cavity ring-down

1044   spectroscopy with laser-current-tuned cavity resonance, Atmos. Meas. Tech., 7, 2014.

1045   Stephens, B. B., Bakwin, P. S., Tans, P. P., Teclaw, R. M., and Baumann, D. D.: Application of a

1046   differential fuel-cell analyzer for measuring atmospheric oxygen variations, J Atmos Ocean Tech, 24,

1047   82-94, 2007.

1048   Sturm, P., Leuenberger, M., Valentino, F.L., Lehmann, B. and B. Ihly: Measurements of CO_2, its stable

1049   isotopes, O_2/N_2, and [222]Rn at Bern, Switzerland, *Atmospheric Chemistry and Physics*, *6*, 1991-2004,

1050   2006.

1051   Tan, Y., Kochanov, R.V., Rothman, L., and Gordon, I.E.:Introduction of water-vapor broadening

1052   coefficients and their temeprature dependence exponents into the HITRAN database, Part 1: CO2,

1053   N2O, CO, CH4, O2, NH3, and H2S, Submitted to Journal of Geophysical Research Atmospheres, 2019,

1054   arXiv:1906.01475 .

1055 Tennyson, J., Bernath, P. F., Campargue, A., Császár, A. G., Daumont, L., Gamache, R. R., Hodges, J. T.,

1056 Lisak, D., Naumenko, O. V., Rothman, L. S., Tran, H., Zobov, N. F., Buldyreva, J., Boone, C. D., De Vizia,

1057 M. D., Gianfrani, L., Hartmann, J.-M., McPheat, R., Weidmann, D., Murray, J., Ngo, N. H., and

1058 Polyansky, O. L.: Recommended isolated-line profile for representing high-resolution spectroscopic

1059 transitions (IUPAC Technical Report), 86, 1931–1943, 2014.

1060 Tohjima, Y.: Method for measuring changes in the atmospheric O-2/N-2 ratio by a gas

1061 chromatograph equipped with a thermal conductivity detector, J Geophys Res-Atmos, 105, 14575-

1062 14584, 2000.

1063 Tran, H., Turbet, M., Hanoufa, S., Landsheere, X., Chelin, P., Ma, Q., Hartmann, J.: The CO_2–

1064 broadened H_2O continuum in the 100–1500 cm-1 region: Measurements, predictions and empirical

1065 model, Journal of Quantitative Spectroscopy and Radiative Transfer, 230, 75-80, 2019.

1066 Valentino, F. L., Leuenberger, M., Uglietti, C., and Sturm, P.: Measurements and trend analysis of O_2,

1067 CO_2 and $\delta 13C$ of CO_2 from the high altitude research station Junfgraujoch, Switzerland — A

1068 comparison with the observations from the remote site Puy de Dôme, France, Sci Total Environ, 391,

1069 203-210, 2008.

1070 Varghese, P. L. and Hanson, R. K.: Collisional narrowing effects on spectral line shapes measured at

1071 high resolution, Appl. Opt., 23, 2376-2385, 1984.

1072 Wójtewicz, S., Cygan, A., Masłowski, P., Domysławska, J., Wcisło, P., Zaborowski, M., Lisak, D.,

1073 Trawiński, R. S., and Ciuryło, R.: Spectral line-shapes of oxygen B-band transitions measured with

1074 cavity ring-down spectroscopy, Journal of Physics: Conference Series, 548, 012028, 2014.

1075 Wolf, P. G., Parthasarathy, G., Chen, J., O'Connor, H. M., Chia, N., Bharucha, A. E., and Gaskins, H. R.:

1076 Assessing the colonic microbiome, hydrogenogenic and hydrogenotrophic genes, transit and breath

1077 methane in constipation, Neurogastroent Motil, 29, 2017.

1078   Zellweger, C., Forrer, J., Hofer, P., Nyeki, S., Schwarzenbach, B., Weingartner, E., Ammann, M., and

1079   Baltensperger, U.: Partitioning of reactive nitrogen (NO$_y$) and dependence on

1080   meteorological conditions in the lower free troposphere, Atmos. Chem. Phys., 3, 779-796, 2003.

1081